

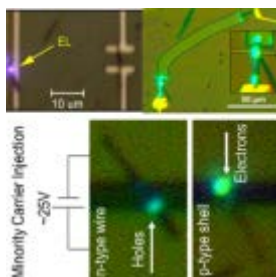
## Optoelectronic properties of single and array of 1-D III-nitride nanostructures: An approach to light-driven device and energy resourcing

Avinash Patsha,<sup>1</sup> Sandip Dhara,<sup>1,\*</sup> Surojit Chattopadhyay,<sup>2,3</sup> K. H. Chen,<sup>4,5</sup> L. C. Chen<sup>5</sup>

<sup>1</sup>Surface and Nanoscience Division, Indira Gandhi Centre for Atomic Research, Homi Bhabha National Institute, Kalpakkam-603102, India. <sup>2</sup>Institute of Biophotonics, National Yang Ming University, Taipei 112, Taiwan. <sup>3</sup>Biophotonics and Molecular Imaging Research Center (BMIRC), National Yang Ming University, Taipei 112, Taiwan. <sup>4</sup>Institute of Atomic and Molecular Sciences, Academia Sinica, Taipei 106, Taiwan. <sup>5</sup>Center for Condensed Matter Science, National Taiwan University, Taipei 106, Taiwan

Submitted on: 28-Nov-2017 Accepted and Published on: 24-Apr-2018

### ABSTRACT



One dimensional (1-D) group III-nitride nanostructures are important components of optoelectronic devices owing to its unique feature of unidirectional carrier flow, and efficient electrical connectivity. The group III-nitride materials are attractive for the application as low power white, and blue-green light sources provide a green and extended operational life. We discuss the luminescence phenomena observed in single or arrayed 1-D III-nitride nanostructures including quantum wells. The role of these 1-D nanostructures is also reviewed in the field of 'green' energy generation, namely hydrogen source in fuel cells, the photoelectrochemical workhorse in renewable energy resourcing, and in solar cells.

*Keywords: III-nitrides, one-dimensional nanostructures, nanolaser, hydrogen generation, solar cell*

### INTRODUCTION

The last two decades had experienced considerable progress in the fabrication of low-dimensional semiconductor systems where only a few systems warrant study of material properties in details for imminent future applications. In low dimensional

semiconductors, since excitons are confined in either of the spatial directions on a length scale comparable to the exciton Bohr radius, many interesting phenomena are expected, namely, the discrete electronic energy band structure, large blue shift of the bandgap energy, and high optical nonlinearity.<sup>1</sup> These characteristic properties of semiconductor nanostructures at low dimensions attract an enormous amount of interest for optoelectronic applications. In the age of quantum information, understanding the nature of excitons and polarons in terms of the dimensionality is an important subject. Electronic states, belonging to few atoms in III-nitride nanomaterials, which mostly take part are relevant for many quantum phenomena such as single electron spin dynamic,<sup>2</sup> photon emission,<sup>3</sup> and others; thus necessitating a detailed evaluation of their individual electronic band structures (influencing absorption or emission of photon), and lattice modes (phonon).

Corresponding Author Name: Sandip Dhara  
Address: Surface and Nanoscience Division, IGCAR,  
Kalpakkam-603102, India  
Tel: +91-44-27480347  
Email: dhara@igcar.gov.in

Cite as: *J. Mat. NanoSci.*, 2018, 5(1), 1-22.

©IS Publications ISSN 2394-0867 <http://pubs.iscience.in/jmns>

The optical properties of single or arrayed nanostructures are always sought after for understanding the real effect of size down to the quantum confinement limit. The subject was dealt by Sugisaki,<sup>4</sup> mainly for zero dimensional (0-D) quantum dots (QDs) in the early years of the present century. With a little improvisation of macro to the micro-setup arrangement, he could demonstrate individual luminescence features of self-assembled QDs. He could even address the features of single QDs with a simple technological innovation.<sup>5</sup> The number of clusters excited through the macroscopic setup is estimated to be about  $10^3$ - $10^6$  with 100  $\mu\text{m}$  focusing diameter of the excitation source for a typical areal nanostructure density of  $10^7$ - $10^{10}$   $\text{cm}^{-2}$ . In order to select and probe a signal from a single nanostructure, a simple method is adopted to study the optical properties through an objective lens of a microscope, which is known as the micro-Raman or photoluminescence (PL) measurements. As a matter of fact, a sub-micron spatial resolution of  $\sim 350$  nm can be achieved with an excitation wavelength of 514.5 nm and an objective of 100X having a numerical aperture of 0.9, which are easily adoptable in present days. Thus one can reduce the number of contributing nanostructures by a considerable amount and down to a single one on a regular basis in the laboratory.

However, 1-D nanostructures stole the lime light with its advantage of easy handling, as compared to nanoclusters, while retaining the features of low dimensionality with the higher surface to volume ratio than that for the 2-D nanostructures. The 1-D nanostructures found applications in numerous fronts of electrical, electronic, optical, sensor, including optoelectronic devices.<sup>6</sup> As a matter of fact, dispersion of single nanostructure in 1-D or quasi 1-D and subsequent microscope assisted spectroscopic studies are routine today. The sub-group of III-nitride nanostructures in 1-D is particularly important in sensor and optoelectronic device applications because of its distinctive characteristic of the unidirectional flow of carrier and ease in getting electrical connectivity. The III-nitrides, such as AlN, GaN, InN and its alloys, are attractive for their ionic nature giving rise to the higher chemical stability and encompassing a broad range of direct bandgap value of 6.2 eV (AlN) down to 0.7 eV (InN). In a 'green' approach with efficient utilization of power, the tunability of the bandgap, with a compositional organization, gives rise to the commercial application of white light at low power and with better operational life than the conventional lighting. High mobility in these materials makes it more attractive for the application in high-speed devices where even light can be coupled in the near future. Application as blue diode laser has redefined the commercial space for submicron lithography as well as entertainment world with high-resolution display, printing and data recording. With such a high pitch for III-nitrides, here we like to review the optoelectronic properties of single or arrayed 1-D nanostructures belonging to this class of materials.

### Luminescence Properties as the Prime Objective

It is relevant for us to review reports on light emission from the single and the arrayed III-nitride nanostructures, as the primary promise of these direct bandgap materials is to emit light. This is a great break through from our century-old slavery to Si, which is an indirect bandgap semiconductor having little future in the

coupling or emission of light, although, till date, they are indispensable for electronics. So Si will be the second choice for the use of all-optical communication, as the semiconductor industry has to live up to both fast communication and swift data processing. Effect of the single or the array of III-nitride nanostructures and their differences with the bulk optical properties were understood in terms of the defects present in those materials.<sup>7-9</sup> Optical features in the single GaN NWs with narrow line-width of the excitonic peak avoiding overlapping of the signal in the ensemble nanostructure,<sup>10</sup> and polarization prevailing till room temperature (RT) were also understood.<sup>11</sup> Role of the surface states were also emphasized while dealing with a single nanostructure.<sup>12,13</sup> Unlike their bulk counterpart, the formation of strain free multiple quantum well (MQW)  $\text{In}_x\text{Ga}_{1-x}\text{N}/\text{GaN}$  was demonstrated with optical emission covering a large range of the visible spectrum of electromagnetic emission for a wide range of In composition.<sup>14-16</sup> Light emission properties were demonstrated in MQW structure of core-shell,<sup>17,18</sup> and axial<sup>19</sup> *p-n* junction light emitting diodes (LED) of single III-nitride nanostructures. Overcoming the strong quantum confined Stark effect in lattice-mismatched polar III-nitrides, InGaN nanodisk ensembles embedded vertically in the single and arrayed GaN nanorod *p-n* junction LEDs emitted full-color sub-wavelengths and natural white electroluminescence.<sup>20,21</sup> Apart from the *p-n* junction diode characteristics, the III-nitride nanostructures also find promising applications in lasing activities. The most important part of the single nanowire (NW) lasing either in an optically pumped system of undoped GaN NW,<sup>22</sup> or the MQW (InGaN/GaN)<sup>23</sup> configuration raised the limit of expectation in these nanostructures. However, a nonpolar surface was efficiently exploited to demonstrate bright far-field emission in pure GaN NWs,<sup>24</sup> for the first time. A nonpolar surface in III-nitrides is known to reduce the effect of electrical polarization, which influences the external quantum efficiency of the emission process.<sup>25</sup>

### Influences of Optical Phonons

The vibrational properties of single and the array of III-nitride nanostructures are essential to understand the detailed structural properties, which eventually affect the optical properties. Reports for spectroscopic studies of single GaN,<sup>26</sup> and InGaN/GaN MQW<sup>27</sup> nanostructures in the sub-diffraction limit using plasmonic nature of the noble metal coated tip-enhanced Raman spectroscopy (TERS) have been reviewed for a limited number of studies, which are reported in the literature. However, there is enough scope to study vibrational properties of a single III-nitride nanostructure in the sub-diffraction limit. Unlike the case in thin films, variable pathways of dopant incorporation in nanowires lead to the nonuniform distribution of dopants along the radial or axial direction of a single nanowire. Apart from the doping process, the type of dopant and the resultant defects in single nanowires with various sizes seriously influence the electrical and optical characteristics of single nanowire devices.<sup>24,28</sup> The localized effects induced by inhomogeneous incorporation of impurities in single NWs can be studied using TERS in the sub-diffraction limit.<sup>29</sup>

We intend to look into the surface optical (SO) phonon modes, as surface structures are detrimental to the optical properties of the nanostructures. Atomic disorders on the surface perturb the momentum conservation of the surface atoms so that the vibration of the SO mode can be intensified.<sup>30</sup> The SO mode is monitored in 1-D single or ordered array of III-nitride nanostructures for understating the surface disorder which has an impact in the excitonic emission process.<sup>31,32</sup> In this context, we may like to mention that heterostructures of III-nitrides leave enough room for the surface disorder to be present in the system.<sup>33,34</sup> Overall, the impact of stress,<sup>35</sup> and polarization on luminescence measurements in single III-nitride nanostructures are also reviewed for understanding their crystalline orientation in a non-destructive spectroscopic technique.<sup>36-38</sup>

### Role as Photodetector and Beyond

We would like to discuss the capability of the single 1-D nanostructures of III-nitrides as photodetectors by establishing their characteristics with the reception of light in ultra thin devices. In nanostructure based detectors, a thinner absorption layer makes carrier transit time shorter leading to high detector speeds but compromising the efficiency of the device to some extent. Role of the crystalline defects, and surface states in controlling the persistent photocurrent (PPC) effect, originating due to carrier trapping resulting into long recombination time, have been discussed.<sup>39,40</sup> Size-dependence of PPC is also reported in GaN NWs having polar side walls with a strong effect of surface band bending (SBB).<sup>41</sup> Moreover, strain related issues, out of composition inhomogeneity at the nanoscale, can be better handled for the detector device fabrication. However, one has to take care of different configurations for improvement of the efficiency in these devices by enhancing absorption of photons, namely, waveguide-based detectors or for that matter adopting resonant structures in designing the photodetector. One has to see how these challenges are met in the nanoscale devices along with the issue of complex integration process with nanoscale electronic components. The subject is well reviewed in a recent article.<sup>42</sup> In the present article, however, we are likely to address some of the concerns of the authors. The 1-D NW based device, with unidirectional flow of current and large surface area, leads to high responsivity for advanced sensor and detector applications.<sup>43</sup> Role of nonpolar III-nitride NWs,<sup>44</sup> and its QW structures<sup>45</sup> have been discussed at length. Consequence of Joule self-heating is also elaborated in the context of producing high photocurrent in a photodetector.<sup>46</sup> Coupling of light, coming out from a single NW based LED, and in the use of single NWs as detector is the ultimate to design for all light driven devices. Thus, the story should not end in understanding the process of emission alone, as the light has to be coupled also for an all-optical device.<sup>47,48</sup> Use as photodetector, thus will establish the credential for these III-nitride based NWs to be used as all light driven devices further.

### Energy Resourcing: Photoelectrochemical Properties

Photoelectrochemical (PEC) properties, where the specific 1-D nanostructure systems of III-nitrides have been used for H<sub>2</sub> generation by splitting of water with the absorption of light in solar-fuel applications, are discussed for both the catalyst free,<sup>49-51</sup>

and catalyst assisted,<sup>52</sup> III-nitride nanostructures. Two methods of photocatalysis and photoelectrolysis, which involve PEC process, have been applied to generate the H<sub>2</sub> by utilizing the semiconductors with the band-gap energy above 2 eV as light absorbers. The light assisted water splitting by semiconductors occurs at first with the excitation of electron-hole (*e-h*) pairs by absorption of incident photons at band edges. During the photocatalysis, the photo-generated electrons and holes separately diffuse to the surface of photocatalysts to perform the reduction and oxidation reactions of water for generation of hydrogen and oxygen, respectively. Both hydrogen and oxygen can be generated at the same catalyst. However, in the PEC process, the generation of hydrogen and oxygen can be separated by cathode and anode, respectively. To achieve overall water splitting, the conduction band minimum of the semiconductor has to be more negative than the reduction potential of H<sup>+</sup>/H<sub>2</sub> (0 V vs normal hydrogen electrode (NHE)) and the valence band maximum has to be more positive than the oxidation potential of O<sub>2</sub>/H<sub>2</sub>O (1.23 V vs NHE).

The process of PEC water splitting involves the conversion of solar energy into chemical energy within a cell containing two electrodes, immersed in an aqueous electrolyte. Out of two electrodes, at least one is made of a semiconductor with a bandgap of minimum 2 eV. The *n*-type semiconductor can function as the photo-anode, and *p*-type semiconductor can serve as photo-cathode. A metal can be used as a counter electrode in the PEC cell. When *n*-type semiconductor is used as a photo-anode the internal electric field produced by SBB, due to the depletion layer formed at the semiconductor/electrolyte interface, will facilitate the separation of photo-generated electrons and holes. This may be achieved through modification of the potential at the electrode/electrolyte interface. The electrons transport to the cathode through the diffusion process and react with protons to generate hydrogen (2H<sup>+</sup> + 2e<sup>-</sup> → H<sub>2</sub>), while the holes accumulate on the surface of the photo-anode and react with water molecules to produce oxygen (H<sub>2</sub>O + 2h<sup>+</sup> → 2H<sup>+</sup> + 1/2O<sub>2</sub>).

With the chemical stability of the ionic bonds in the III-nitride system in the corrosive photocatalysis process and having more negative potential of the N 2*p* orbital, as compared to that of the O 2*p* orbital, III-nitride often possess required minimum bandgap which can cover a major part of the solar spectrum.<sup>53</sup> These properties made the III-nitride semiconductors, with tunable bandgap, more attractive over large bandgap metal oxides and oxynitrides for water splitting involving ions with filled or empty *d*-shell bonding configurations.<sup>52</sup> Couple of theoretical predictions and experimental results also drew attention for water splitting to be favoured on Ga-terminated polar surface and nonpolar (10-10) surface of GaN.<sup>54-56</sup> In addition, to enhance the PEC hydrogen generation performance further, there are various approaches including bandgap engineering, suitable doping, and nanostructure formation and additional catalyst decoration of photo-electrodes have been followed. The separation of photo-generated *e-h* pairs would be more efficient and fully utilized in NWs, due to the effect of SBB, by tuning the NW diameter comparable to the width of the depletion layer. Mg-doped *p*-GaN NWs with controlled surface charge was also reported to achieve very efficient and extremely stable water splitting.<sup>57</sup>

### Energy Resourcing: Photovoltaic Properties

Last but not the least, the application of homojunction and heterojunctions of single and arrays of III-nitride nanostructures for photovoltaics have been discussed as the most important optoelectronic application in the search for 'green' energy. The III-nitrides are also having interesting properties required for photovoltaic applications including the ability to tune the bandgaps of AlGaN in the deep UV regime (3.4-6.2 eV), and InGaN across a major part of the solar spectrum (0.7–3.4 eV).<sup>58</sup> The high degree of radiation resistance,<sup>59</sup> and optical absorption coefficient ( $\sim 10^5 \text{ cm}^{-1}$ )<sup>60</sup> make III-nitrides potential candidate for photovoltaic applications even in outer space with the highest predicted the efficiency of 80%. Wide bandgap GaN nanorod arrays on the cell surface can act as an antireflection layer to reduce the visible optical loss. Heterojunction solar cells of III-nitride systems with Si were of natural interest.<sup>61</sup> The coaxial *p-i-n* junctions, exploiting the III-nitrides along with either compound,<sup>62</sup> or MQW nanostructures,<sup>63,64</sup> as intrinsic *i*-layer was also demonstrated.

### LUMINESCENCE PROPERTIES OF INDIVIDUAL AND ARRAYED NANOWIRES

#### Effect of Single or Arrayed Nanostructures

While looking into the single or the array of 1-D nanostructures, our initial objective was to specify any major difference between the optical properties of individual and arrayed nanostructures. In a simple study,<sup>7</sup> using micro-PL setup, it was found that the PL spectra for individual GaN NW was dominated by a sharp UV peak around  $\sim 343 \text{ nm}$ , and was devoid of the yellow band signifying nearly defect free structure. The NWs were grown in the catalyst free process using plasma-assisted molecular beam epitaxy (PA-MBE). A broad yellow luminescence (YL) band around 2.22-2.3 eV and defect-related band centered around 3.36 eV were observed only for the coalesced NWs. Because of the photoinduced surface desorption of oxygen, the PL spectra were found to be sensitive to the UV illumination. The effect was stronger in individual NWs owing to the larger surface-to-volume ratio as compared to that for the coalesced NWs. In a separate study, the YL band was correlated to the presence of threading dislocation in an epitaxially grown array of GaN NWs

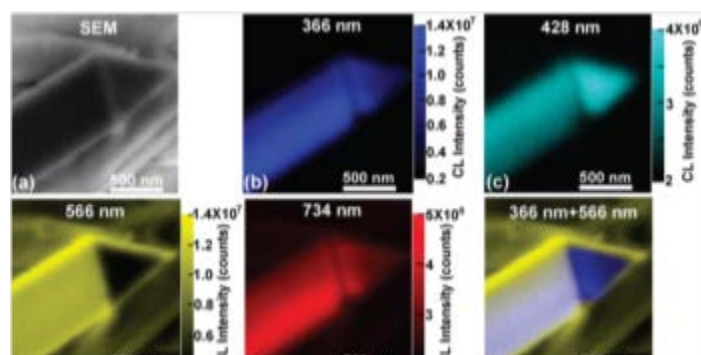


**Figure 1.** (a) SEM image showing the triangular cross-section of a GaN NW; (b-e) monochromatic CL images of the same NW at 366, 428, 566, and 734 nm; (f) composite image of (b) and (d). (Reprinted with permission from Ref. 12, Copyright © 2010 American Chemical Society)

in carbon free condition,<sup>8</sup> grown in the conventional chemical vapor deposition (CVD) technique using vapor-liquid-solid (VLS) mechanism with Au as a catalyst. The insertion of Al/Au layers in GaN/*c*-Al<sub>2</sub>O<sub>3</sub> interface significantly removes the threading dislocation and depresses the YL band. A sharp peak alone in the UV range (3.36 eV) can be observed in cathodoluminescence (CL) measurement.

Moreover, we could also get an understanding of thickness and size effect on luminescence properties in Ni catalyst assisted metal-organic chemical vapor deposited (MOCVD) 1-D GaN NW,<sup>12</sup> using spot-CL measurements. Intensities of blue luminescence (BL) at 2.9 eV, red luminescence around 1.7 eV and band edge emission at  $\sim 3.4 \text{ eV}$  were found to progressively increase as the NW diameter approached the bulk limit. The YL band at  $\sim 2.2 \text{ eV}$ , however, was predominant on the surface layer (Figure 1). The surface layer thickness sensitivity of the YL band was found to increase progressively with increasing NW diameter as measured in the spot-CL measurement of GaN NW having a triangular cross-section.<sup>12</sup>

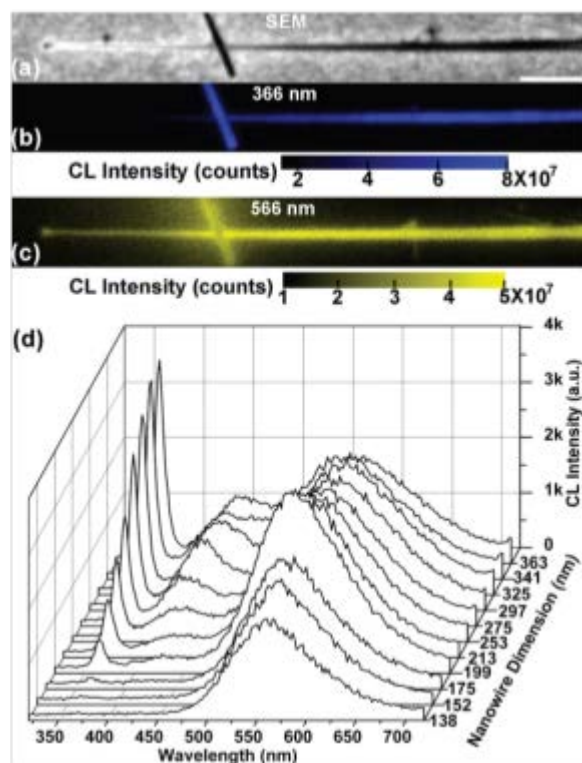


**Figure 2.** (a) SEM image showing a tapered GaN NW. The scale bar is 0.5  $\mu\text{m}$ ; (b,c) The corresponding monochromatic CL images at 366 and 566 nm; (d) Spot-mode CL spectra obtained along the center line of the NW are plotted as a function of the NW dimension (width). (Reprinted with permission from Ref. 12, Copyright © 2010 American Chemical Society)

The band edge luminescence was interestingly found to quench below a critical dimension of the NW (Figure 2), and the phenomenon was attributed to the surface accumulation of mobile point defects, comprising of isolated Ga vacancies, at the surface acting as an electronic sink. For an ensemble of preferentially oriented GaN NWs, not an array, the origin of the blue-shift of the

band edge PL peak in *a*-axis GaN NWs with respect to the *c*-axis GaN NWs was explored,<sup>13</sup> and these surface trap states were found to be a prime factor. The findings were different than earlier reports that mentioned the effect of strain,<sup>65</sup> or built-in polarization in the ionic bonded GaN<sup>25</sup> to be responsible for the blue shift. The results were nevertheless important as the role of the surface effects were elucidated for UV based GaN optoelectronic devices.

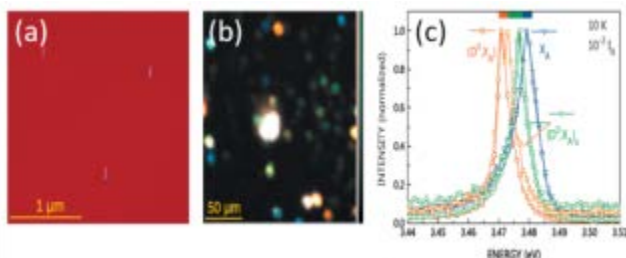


**Figure 3.** (a) Bird's-eye view (30°) of the low-density edge region of the NW ensemble under investigation. The raw SE micrograph is color coded to enhance the material contrast between GaN and Si. Evidently, no parasitic growth takes place in between the free-standing NWs. (b) Trichromatic PL intensity map, at 10 K, of the low-density edge region of the NW ensemble under investigation. The spectral range characteristic for bulk like and surface donor-bound excitons is displayed in red and green, respectively, while the free-exciton transition is decoded in blue. (c) Representative PL spectra from six individual NWs within the map displayed in (b). The spectral range for each of the transitions is denoted at the top. (Reprinted with permission from Ref. 10, Copyright © 2010 American Physical Society)

Excitonic transition with line width below 300  $\mu\text{eV}$  was reported in catalyst free PA-MBE grown single GaN NWs dispersed on Si(111).<sup>10</sup> At the same time, the excitonic energy was reported at higher energies above the donor-bound exciton in the bulk GaN. With such a low line width value, a high crystal quality was conceived with point defects and impurities driven to the NW sidewalls during growth. The broadening of about 3 meV was observed for the NW array. For the array, however, the broadening was shown to be because of the energy dispersion of bound-exciton states as a function of their distance from the surface (Figure 3). The broadening in case of single NWs was non-intrinsic in nature. Polarized PL spectra of single GaN NWs were reported<sup>11</sup> to have different anisotropy for  $\pi$  and  $\sigma$  polarization cases. Unlike bulk or ensemble NW system, interestingly the polarization anisotropy was maintained till room temperature (RT) from 4 K. The role of single or arrayed nanowires is clearly evident from these studies to resolve the complexity in understanding of the luminescence due to point and extended defects, surface states, crystalline quality and orientation, observed in GaN.

#### Light Emission from Quantum Wells and Core-shell 1-D Nanostructures

Hyperspectral CL imaging of single MOCVD grown InGaN/GaN-based nanorods containing multiple quantum wells (MQWs) was reported with very high spatial and spectral resolution.<sup>14</sup> An AlN buffer layer was used in the growth process

to reduce strain related defect in these nanostructures. The MQW emission energy varies by approximately 18 meV across the region containing the wells. However, there was no variation of the emission energy of the GaN below the MQWs signifying negligible strain variation along the rod axis in the QW layer (Figure 4). In a seminal report, the growth of single-crystalline  $\text{In}_x\text{Ga}_{1-x}\text{N}$  NWs with a compositional range encompassing  $x = 0$  to 1 was demonstrated for the first time in a low temperature halide chemical vapor deposition process.<sup>15</sup> The striking feature was a tunable emission from the near-ultraviolet to the near-infrared region (Figure 5). The complete composition tunability was possible due to the low growth temperature and the NW morphology enabling growth with minimum strain.<sup>16</sup> The latter was primarily responsible for the phase separation observed in thin film morphology.

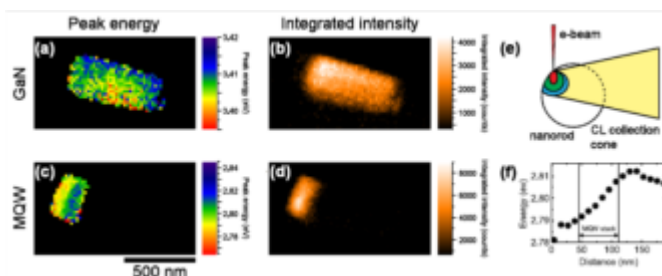


**Figure 4.** Room temperature CL maps gained by fitting the hyperspectral data set in figure 2(b) of Ref. 14 with Voigt and Gauss functions for the GaN and MQW emission peaks, respectively: (a) peak energy and (b) integrated intensity maps of the GaN band edge emission and (c) peak energy and (d) integrated intensity maps of the MQW emission. Using the spectral information gained by peak fitting it is possible to identify the spatial origin of the two peaks and map shifts in their energy. The MQW emission is located on the left-hand side corresponding to the top of the nanorod, whereas the GaN emission originates from the area below this region. The map of the GaN peak shows a negligible energy shift along the nanorod axis suggesting no variation in strain. However, the map of the MQW emission displays a small redshift towards the top surface of the nanorod. (e) Schematic diagram showing the influence of self-absorption. Light generated on the left-hand side of the rod has to pass through the nanorod to reach the detection optics. The excitation volume induced by the electron beam is also shown. (f) Line scan through the MQW emission energy map in (c) showing a small redshift along the axis towards the top of the nanorod. (Copyright Ref. 14@2013; Open Access)

MOCVD grown *n*-GaN/InGaN/*p*-GaN doped core/shell/shell (CSS) NW heterostructures showed strong emission from the InGaN shell centered at 448 nm, and 367 nm from the *n*-GaN NW core.<sup>17</sup> A blue LED with bright blue emission from the InGaN shell was also demonstrated (Figure 6).<sup>17</sup> The same group reported,<sup>18</sup> LED properties of MOCVD grown core/multishell (CMS) NW radial heterostructures of *n*-GaN core and  $\text{In}_x\text{Ga}_{1-x}\text{N}/\text{GaN}/\text{p-AlGaIn}/\text{p-GaN}$  shells using the variation of In mole fraction for tuning the emission wavelength from 365 - 600 nm with high quantum efficiencies (Figure 7). The CSS and CMS structures were projected as prospective candidates for single NW based multicolor LEDs and nanophotonics, including multicolor lasers.

The PL study of homoepitaxially grown *p*-type Mg-doped GaN shells on *n*-GaN NWs core NWs in the halide vapor phase epitaxy (HVPE) technique showed the presence of sub-bandgap features belonging to the acceptor states.<sup>66</sup> Electroluminescence (EL) study affirmed the presence of electrically active holes being injected in the *n*-GaN core and electron injection in the *p*-type shell was also evidenced. In a separate study, EL of *n*-GaN NW on *p*-GaN thin film homojunction passivated with a thin layer of SiO<sub>2</sub> showed emission at 365 nm. The scheme looked attractive as a batch fabrication process for electrically injected nanoscale UV light sources with reliable yields was possible.<sup>19</sup> Wide range of tunable light emissions from UV to IR could be possible by stress free tuning of composition and dopant in core/shell nanostructures with homo and heterojunctions.

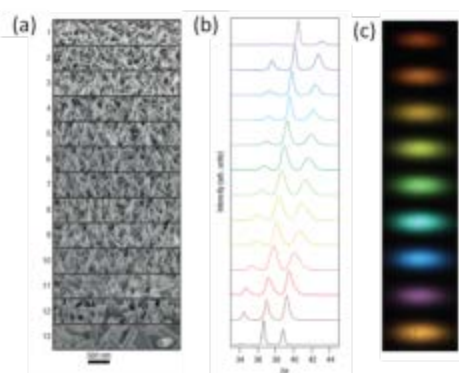


**Figure 5.** Wire morphology and XRD at varying InGaN composition ( $x = 0-0.6$ ). (a) SEM images of the NW morphology, with increasing In concentration from images 1 to 13. The wire morphology changes most noticeably in 10–11 from the smaller to larger wires at around 75–90% In. (b) 100, 002 and 101 XRD peaks from left to right of the NWs, with increasing In concentration from images 1 to 13. (c) corresponding colour CCD images. (Reprinted by permission from Ref. 15, Copyright © 2007 Nature Publication Group)

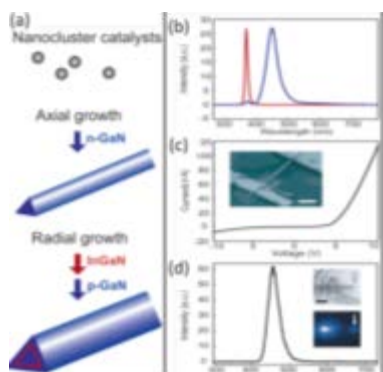


**Figure 6.** (a) Synthesis of CSS NW heterostructures. Catalytic metal nanoclusters lead to one-dimensional GaN NW (blue) growth via a VLS mechanism. Subsequently, conditions are changed to favor uniform surface deposition, which enables growth of controlled thickness InGaN (red) and GaN (blue) shells epitaxially on the GaN NW cores. Optoelectronic properties of *n*-GaN/InGaN/*p*-GaN CSS NWs. (b) Normalized PL spectra obtained from single *n*-GaN (red) and *n*-GaN/InGaN/*p*-GaN CSS (blue) NW. (c) Current vs voltage data recorded on a *n*-GaN/InGaN/*p*-GaN CSS NW device. Inset: field emission SEM image of a representative CSS NW device prepared using the FIB technique to selectively etch the outer shells from one end (lower right) of the CSS NW prior to contact deposition. Scale

bar is 1  $\mu\text{m}$ . (d) EL spectrum recorded from a forward-biased CSS *p*-*n* junction at 7 V. Insets: bright field (upper) and EL (lower) images of a CSS structures. The EL image was recorded at 4 K with a forward bias of 12 V. White arrows in both images highlight the end of the CSS NW. Scale bar is 2  $\mu\text{m}$ . (Reprinted with permission from Ref. 17, Copyright © 2004 American Chemical Society)

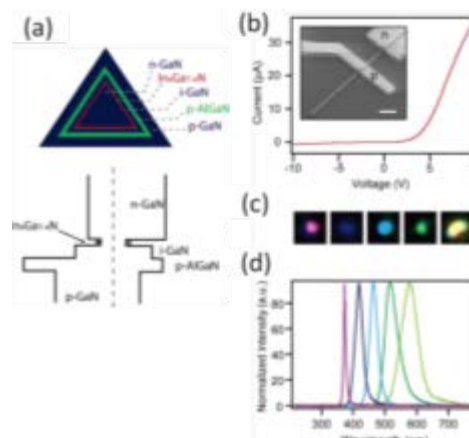


**Figure 7.** (a) Cross-sectional view of a CMS NW structure and the corresponding energy band diagram. The dashed line in the band diagram indicates the position of the Fermi level. (b) Current versus voltage data recorded on a CMS NW device. Inset: field emission scanning electron microscopy image of a representative CMS NW device. Scale bar is 2  $\mu\text{m}$ . (c) Optical microscopy images collected from around *p*-contact of CMS NW LEDs in forward bias, showing purple, blue, greenish-blue, green, and yellow emission, respectively. (d) Normalized EL spectra recorded from five representative forward-biased multicolor CMS NW LEDs. (Reprinted with permission from Ref. 18, Copyright © 2004 American Chemical Society)

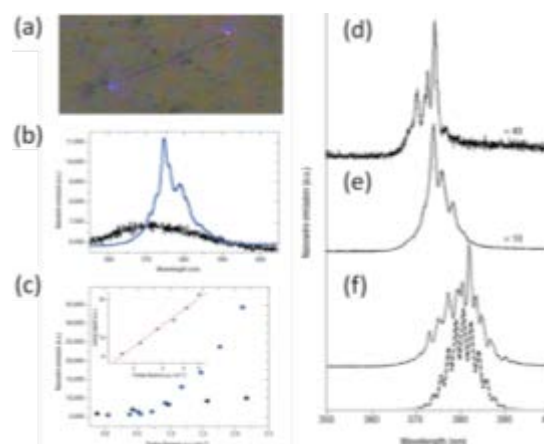


**Figure 8.** Individual, isolated GaN NW laser (a) Far-field image of a single GaN nanolaser. The sample was back-illuminated with a lamp to show the structure, and the NW was excited with about  $3\mu\text{Jcm}^{-2}$ . The colour indicates laser emission at the ends of the NW (b) Spectrum of photoluminescence (black) using 1 mW continuous-wave excitation and lasing (blue) using about  $1\mu\text{Jcm}^{-2}$  pulsed excitation (c) Power dependence of the lasing near threshold (blue) and of photoluminescent emission from a non-lasing region (black). Inset: logarithmic plot of lasing power dependence. Spectral power dependence of nanolaser emission: (d)–(f) NW laser emission at 0.7, 1.2 and 2  $\mu\text{Jcm}^{-2}$ , respectively. Dashed curve, simulation of NW resonator spectral properties, considering equal contributions of one- and two-pass stimulated emission. (Reprinted by permission from Ref. 22, Copyright © 2002 Nature Publication Group)

### Lasing in Single 1-D Nanostructures

An early realization of electron-injected NW-based UV-blue coherent light sources was demonstrated from the RT lasing action in a single crystalline Ni catalyst assisted VLS grown GaN NW with a threshold pumping power of  $\sim 1 \mu\text{J}\cdot\text{cm}^{-2}$  (Figure 8). Both near- and far-field studies were performed for understanding the spectral nature and waveguide mode at RT.<sup>22</sup> Observed red shift of the emission line with the increasing pump power established the electron-hole plasma as responsible mechanism for the cavity gain at RT. An optically pumped RT lasing was also reported<sup>67</sup> (Figure 9) in MOCVD grown nonpolar GaN NWs with a threshold pumping power of  $22 \text{ mJ}\cdot\text{cm}^{-2}$ . The excitonic and the photonic confinement within coaxial quantum-wire-in-optical fibers (Qwof) formed by spontaneous phase separation of MBE grown Al-GaN at the nanometer scale led to the observation of quantum wire lasers.<sup>68</sup> Far-field bright violet emission spots (Figure 10) from nonpolar oxygen free GaN NWs, grown in a unique VLS assisted CVD, was observed because of the formation of the single-mode waveguide in these samples.<sup>24</sup> A bright emission in the far field was realized, for the first time, exploiting the reduced polarization-induced electric fields effect in nonpolar GaN nanostructures affecting the external quantum efficiency of light emission.<sup>24</sup> Triangular MOCVD grown MQW (InGaN/GaN)<sub>n=3,13,26</sub> with GaN NW as core and InGaN well thicknesses of 1–3 nm yielded lasing over a broad range of wavelengths at RT.<sup>23</sup> Optical pumping with threshold varying with  $n$  for single MQW NW showed lasing with InGaN composition-dependent emission from 365 to 494 nm (Figure 11). The RT lasing and waveguide nature in single nanowires with a tunable emission wavelength in MQW are shown to be promising developments as sources of light from nanoscale elements.

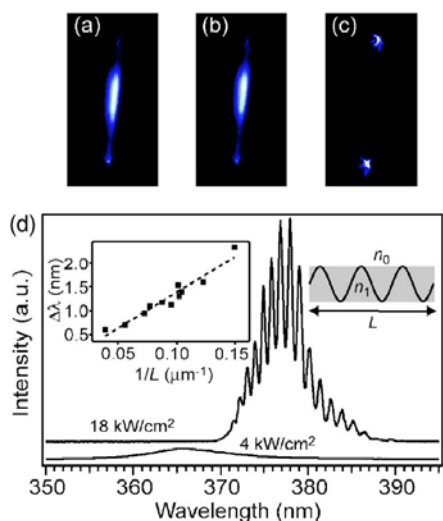


**Figure 9.** Power-dependent PL studies of  $n$ -type HT GaN NW cavity properties. Images of a single NW excited with (a)  $4 \text{ kW}/\text{cm}^2$ , (b)  $17 \text{ kW}/\text{cm}^2$ , and (c)  $66 \text{ kW}/\text{cm}^2$ . (d) PL spectra recorded at the end of  $13 \mu\text{m}$  long NW for  $4 \text{ kW}/\text{cm}^2$  and  $18 \text{ kW}/\text{cm}^2$  power densities showing Fabry-Pérot cavity modes with average mode spacing of  $1.1 \text{ nm}$ . Right inset: schematic representation of a longitudinal NW cavity with length  $L$  whose index of refraction,  $n_1$ , is larger than that of surrounding air,  $n_0$ . Left inset: mode spacing vs inverse NW length. (Reprinted with permission from Ref. 67, Copyright © 2005 American Institute of Physics)

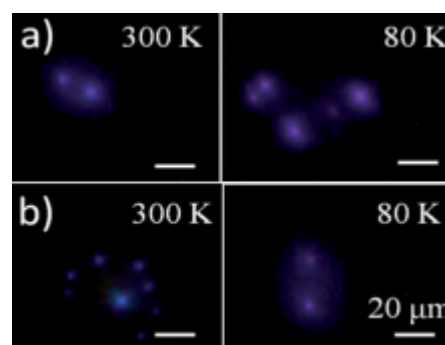


**Figure 10.** Typical optical images of far field bright violet emission spots at  $300 \text{ K}$  and  $80 \text{ K}$  on the NWs of samples with average diameters of (a)  $40$ , and (b)  $55 \text{ nm}$ . Emission spots come out of the ends of the NWs through the available open space while other ends are at the excitation with laser light. (Reprinted with permission from Ref. 24, Copyright © 2013 Royal Society of Chemistry)

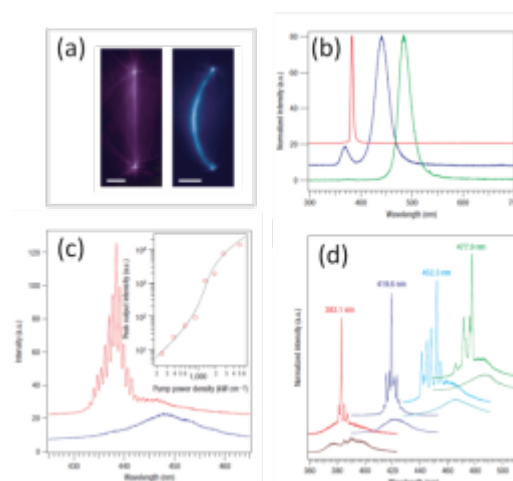


**Figure 11.** MQW NW photoluminescence: (a) Photoluminescence images (false colour) recorded from GaN/In<sub>0.05</sub>Ga<sub>0.95</sub>N (left) and GaN/In<sub>0.25</sub>Ga<sub>0.75</sub>N (right) MQW NW structures. Scale bars are  $5 \mu\text{m}$ . (b) Normalized spectra collected from three representative 26MQW NW structures with increasing In composition; excitation power density  $\sim 150 \text{ kW cm}^{-2}$ . (c) Photoluminescence spectra of a 26 MQW NW recorded at excitation power densities of  $250$  and  $1,300 \text{ kW cm}^{-2}$ , respectively. Spectra are offset for clarity. Inset: Log-log plot of output power versus pump power density. Red open circles are experimental data points and the dashed line is the fit calculated with the rate equations. (d) Normalized photoluminescence spectra collected from four representative 26 MQW NW structures with increasing In composition pumped at  $\sim 250 \text{ kW cm}^{-2}$  and  $\sim 700 \text{ kW cm}^{-2}$ , respectively. Spectra are offset for clarity. (Reprinted by permission from Ref. 13, Copyright © 2008 Nature Publication Group)

The surface plasmon amplification by stimulated emission of radiation (SPASER) is proved to be the potential technique as the source and amplifier of coherent optical and surface plasmon fields for developing the new class of lasers.<sup>69</sup> By utilizing the SPASER technique, metal-oxide-semiconductor (MOS) structure based plasmonic green laser has been demonstrated.<sup>69</sup> The MOS structure consists of a bundle of InGaN/GaN nanorods on a gold plate separated by a thin SiO<sub>2</sub> ( $5 \text{ nm}$ ) dielectric layer. Further, by selecting a proper plasmonic material such as Ag, a plasmonic sub-diffraction nanolaser, operated in continuous-wave (CW)

mode at low-threshold, was developed.<sup>70</sup> The MOS based nanolaser was fabricated by a single InGaN@GaN core-shell nanorod on SiO<sub>2</sub> (5 nm)-spacer layer covered by atomically smooth epitaxial Ag film (28 nm thick). The device having nanocavity formed between plasmonic film and semiconductor nanorod showed highly polarized multiple mode (510, 522 nm) CW lasing at 78 K under varying power densities of optical pumping with a threshold of 3.7 kW/cm<sup>2</sup>. By tuning the In concentration in In<sub>x</sub>Ga<sub>1-x</sub>N@GaN nanorods and replacing SiO<sub>2</sub> gap dielectric layer with high-quality Al<sub>2</sub>O<sub>3</sub> grown by atomic layer deposition (ALD), broadband tunable, single-mode plasmonic nanolasers emitting in the full visible spectrum have been realised recently (Figure 12).<sup>71</sup> Al<sub>2</sub>O<sub>3</sub> dielectric layer, along with atomically smooth Ag film, further reduced the surface plasmon polariton scattering loss, resulting in the ultralow lasing threshold.

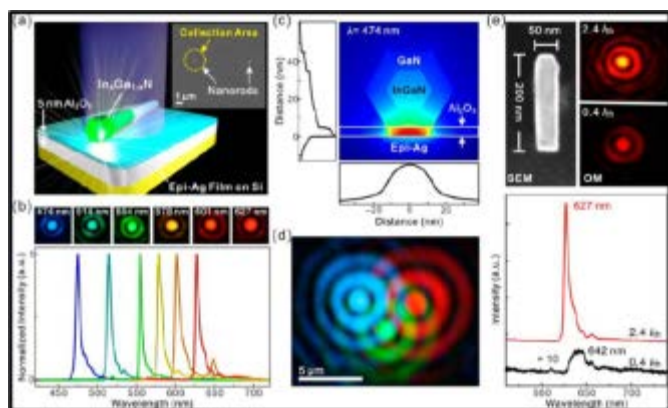


**Figure 12.** All-color InGaN@GaN nanorod plasmonic lasers. (a) Schematic diagram of the nanolaser structure: Single In<sub>x</sub>Ga<sub>1-x</sub>N@GaN core-shell nanorod were dispersed on the Al<sub>2</sub>O<sub>3</sub>-covered epitaxial Ag film. The scanning electron microscopy (SEM) image on the upper right indicates that we can measure the laser emissions from individual single nanorods with a collection area of about 3 μm in diameter using a focused excitation laser beam. (b) All-color, single-mode lasing images observed from single nanorods with an emission line width ~4 nm. (c) The simulated energy density distribution of a blue (474 nm) nanolaser. The resonant field is tightly confined in the 5 nm, low-index ( $n \approx 1.77$ ) Al<sub>2</sub>O<sub>3</sub> gap layer grown by ALD and the plasmonic cavity mode is formed between the nanorod and the epitaxial Ag film. (d) Concurrent RGB lasing from three nanorods placed close to each other. The optical pumping source is a 405 nm, CW semiconductor laser diode with an excitation power density of 3.9 kW/cm<sup>2</sup>. The scale bar represents 5 μm. (e) An ultrasmall plasmonic nanolaser emitting at 627 nm (red) that is pumped below ( $0.4 I_{th}$ ) and above ( $2.4 I_{th}$ ) the lasing threshold. Both the optical images and the emission spectra show that a strong frequency pulling effect occurs during transition from spontaneous emission (642 nm) to lasing (627 nm). (Reprinted with permission from Ref. 71, Copyright © 2014 American Chemical Society)

## LATTICE VIBRATIONAL PROPERTIES OF INDIVIDUAL AND ARRAYED NANOWIRES

### Optical Phonon Studies in Single 1-D Nanostructures

In a unique study of a single GaN NW, using tip-enhanced Raman scattering (TERS), the intensity distribution of a specific, E<sub>2</sub>(high) mode across the NW of diameter 200 nm was shown.<sup>26</sup>

The study indicates the prospect of probing the surface and bulk of the individual NWs by studying the variation of these phonon modes. Subsequently, variations in the chemical composition, charge distribution, strain and the presence of stacking faults leading to different polymorphs close to the surface near the MQW region (Figure 13) in metal-organic vapor phase epitaxy (MOVPE) grown single nonpolar InGaN/GaN MQW nanorods were optically investigated using TERS with a spatial resolution in the sub-diffraction limit.<sup>27</sup> Variation of the In content for the InGaN layer of a few percents was reported with a lateral resolution < 35 nm. The evidence of In clustering and deposition of cubic phase close to QW layers was also reported.<sup>27</sup> A vibrational study carried out on different kinds of impurity (O and Mg) incorporated single GaN NWs using TERS in the sub-diffraction limit, showed the localized effects. The undoped and impurity incorporated GaN nanowires were synthesized using CVD technique in the VLS process.<sup>20,24,25</sup> Unusually strong intensity of non-zone center zone boundary mode around 421 cm<sup>-1</sup> in the undoped and GaN:Mg nanowires show the role of the evanescent field in the absence of major native defects and free

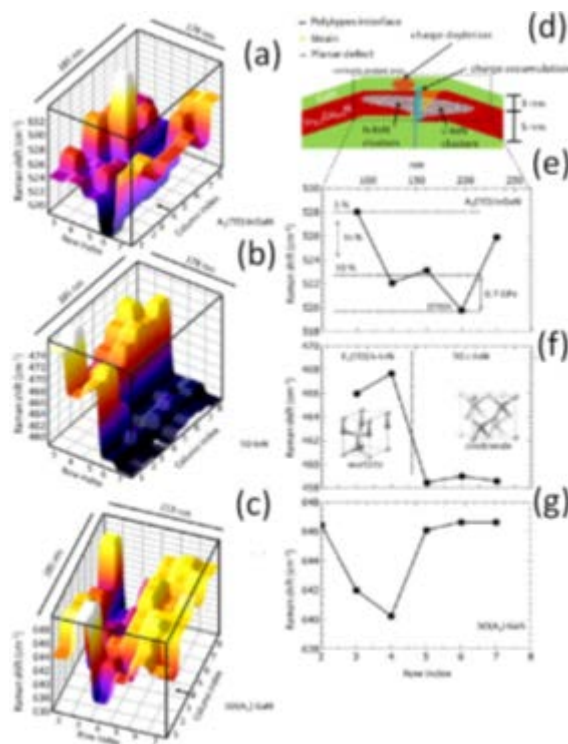


**Figure 13.** (a–c) Three-dimensional visualization of the Raman frequencies of three different modes as a function of the spatial map coordinates ( $r, c$ ). (a) A<sub>1</sub>(TO) mode of InGaN layers, (b) E<sub>1</sub>(TO) and TO modes of the hexagonal and cubic modifications of InN, respectively, and (c) A<sub>1</sub> surface optical (SO) mode of the GaN capping layer. Spatial coordinates without Raman signal of the respective modes are omitted from the maps. The arrows indicate the plotted column (fourth column) in the line scan profiles in e–g. (d) Simplified schematic illustration of the nanorod top region in cross sectional view. (e–g) Raman shift related to the cross sectional scheme in d for the spectra of the line scan along the fourth column of the TERS map. (Reprinted with permission from Ref. 27, Copyright © 2013 American Chemical Society)

carrier-phonon coupling in these nanowires (Figs. 14(a,b)). Observation of local vibrational mode (LVM) around  $656\text{ cm}^{-1}$  pertaining to Mg in GaN NW confirmed the presence of Mg as a dopant in the single GaN nanowires. A strong longitudinal optical (LO) phonon-free carrier coupling was envisaged in O rich GaN nanowires from the observed asymmetry of the  $A_1(\text{LO})$  mode around  $729\text{ cm}^{-1}$  where the generation of carriers are due to the presence of the N vacancy and O point defects (Figure 14c). A vibrational mode corresponds to the oxy-nitride ( $\text{GaO}_x\text{N}_y$ ) phase due to the inhomogeneous inclusion of O in GaN NW has also been identified by the localized study (Figure 14c).

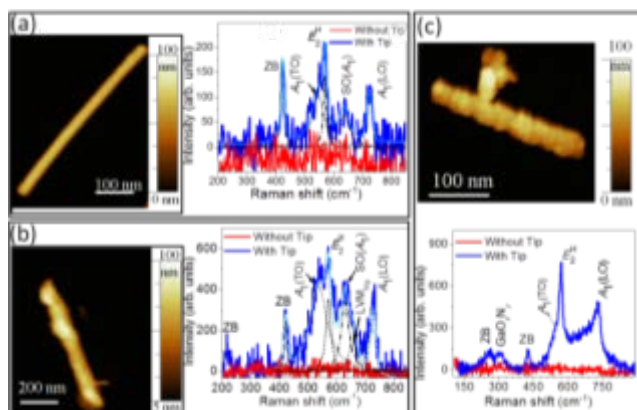


**Figure 14.** Localized vibrational study of undoped and impurity incorporated single GaN NWs by TERS. AFM (left side) and Raman spectra (right side) of (a) undoped and (b) Mg doped GaN NW. (c) AFM (top) and Raman spectra (bottom) of O impurity incorporated GaN NW (Reprinted with permission from Ref. 29, Copyright © 2015 American Institute of Physics)

In a micro-Raman setup, the phase was mapped for single microbelts with GaN nanoprotuded shell on  $\text{Ga}_2\text{O}_3$  core grown in catalyst free CVD technique following vapour-solid (VS) mechanism.<sup>35</sup> The phase mapping allows a non-destructive tool for understanding the growth mechanism of a low symmetric monoclinic  $\text{Ga}_2\text{O}_3$  phase, and a high symmetric GaN phase formation taking place simultaneously as the core and shell, respectively, with a sharp interface. The sharp interface, however, was confirmed in the detailed high-resolution cross-sectional transmission electron microscopic (HRTEM) studies.<sup>35</sup> Radial Raman spectroscopic line scanning along the cross-section of single GaN nanotips, grown in the catalyst free VS process, showed the presence of residual strain at the core.<sup>72</sup> The observed residual strain was due to the preferential crystalline orientation at the core which was different from the bounding surface. Chemical affinity makes Ga diffusion rate lower in the polar surface, with either Ga or N termination than that for the non-polar surface with the negligible chemical interaction of Ga on saturated Ga-N bonds.<sup>73</sup> Hence the growth of the GaN phase was enunciated at the non-polar surface. Assisted with HRTEM analysis, the finding of residual strain at the core resolved the issue of the differential growth dynamic of GaN phase at different crystalline planes present in the polar core and on the non-polar surface of the nanostructure, as the reason for the growth of tip shape. Optical phonons in single III-nitride nanostructures studied by Raman

spectroscopy are prevalent in the conformation of chemical composition and phase inhomogeneity across the nanostructures.

### Surface Optical Raman Modes in Single and Array of 1-D Nanostructures

Polarized micro-Raman study of MBE grown single GaN NW identified the SO mode at  $708.5\text{ cm}^{-1}$ .<sup>31</sup> Surface optic nature of the two peaks, centered near  $700\text{ cm}^{-1}$ , were confirmed for PA-MBE grown GaN columnar nanostructures by varying the dielectric environment and simultaneous polarization, filling factor, incident angle dependent measurements.<sup>32</sup> Two peaks were found because of the anti-crossing of axial and planar surface-related phonons. The same was anticipated for all anisotropic polar semiconductors. Size of the GaN NW and inter-NW separation, leading to a difference in fill factor, were experimentally studied and modeled according to Maxwell-Garnett approximation.<sup>74</sup> The dependence of SO mode frequency with fill factor was found to be dominated by inter-NW dipolar interaction for an array.<sup>74</sup> The splitting of the SO mode was ascribed to the anti-crossing between surface modes with  $A_1$  and  $E_1$  symmetry, due to a deviation of the excitation light from the NW axis. It was also concluded that this splitting was a consequence of the strong optical anisotropy and the polar nature of GaN, and should be present in NWs based materials with similar characteristics. The SO modes originating from the surface defects with enhanced intensity for an undoped and Mg-doped GaN NWs were observed in a localized study by TERS.<sup>29</sup> The SO modes of surface modulated InN,<sup>75,76</sup> GaN NW,<sup>77</sup> and 2-D monolayer of GaN nanobelts,<sup>78</sup> InGaN MQW,<sup>34</sup> and diameter modulated AlN<sup>79</sup> nanostructures with individual surface features were reported with a full review covering details of those nanostructures.<sup>30</sup> In case of the array in MBE grown InN nanorods, we could resolve the growth orientation by simple observation of the distribution of the SO mode at  $561\text{ cm}^{-1}$  and the bulk  $E_1(\text{LO})$  mode at  $589\text{ cm}^{-1}$  over an area.<sup>76</sup> The SO mode alone was observed from the tips with surface irregularities, whereas the bulk LO mode was emanating from the whole array including the tip to differentiate between the aligned and obliquely oriented array (Fig 15). Corresponding to the LO mode imaging, oblique nanowires were observed to be indistinguishable as the whole nanowire responded to LO phonon

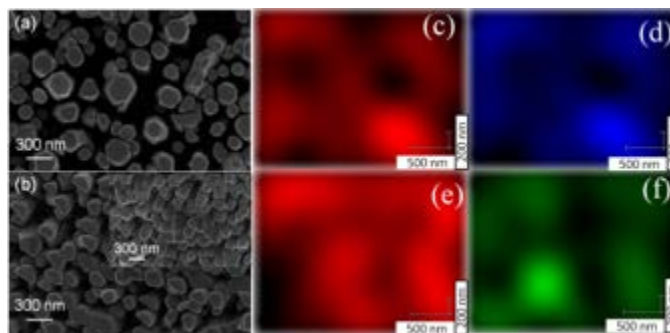


**Figure 15.** FESEM micrographs of (a) vertical and (b) oblique nanorods. Inset in (b) shows the  $60^\circ$  tilted image. Intensity distribution of Raman area mapping using  $E_1(\text{LO})$  and  $\text{SO}(E_1)$  modes of (c, d) vertical and (e, f) oblique nanorods. (Reprinted with permission from Ref. 76, Copyright © 2013 John Wiley & Sons, Ltd.)

mode. On the other hand, LO modes are only visible from the tip of the nanowire in case of aligned nanowires.  $p$ -GaN/[InGaN/GaN]<sub>10</sub>/ $n$ -GaN nanopillars were grown in a top-down technique using Ga<sup>+</sup> assisted focused ion beam (FIB) dry etching of a wafer having same layer arrangement of III-nitrides, and subsequent wet chemical KOH etching for the removal of surface irregularities created during the ion beam process.<sup>34</sup> The presence of InGaN/GaN MQW in an array of  $p$ -GaN/[InGaN/GaN]<sub>10</sub>/ $n$ -GaN nanopillars was realized from the SO Raman studies of a ternary system for the first time.<sup>34</sup> The SO mode in single and arrayed nanostructures of III-nitrides was reviewed elaborately for understanding the surface features in the finite size of the crystallite.<sup>80</sup>

### Polarized Raman Studies

Size dependent Raman study of individual AlN NWs grown in the vapor transport and condensation technique showed a strong anisotropic behavior resulting from an optical antenna effect in small NWs (diameter < 50 nm). The anisotropic Raman effect of single NWs was observed in terms of Raman enhancement. To make a comparison of Raman enhancement of NWs with that of the thin film, a value of Raman enhancement per unit volume; RE =  $[I_{nw} / V_{nw}] / [I_{ref} / V_{ref}]$  has been defined. Here,  $I_{nw}$  represents the measured Raman intensity of NW,  $I_{ref}$  is for high quality thin film,  $V_{nw}$  and  $V_{ref}$  denote the volume of NW and thin film, respectively. Compared to the thin film, ~ 200-fold increase of RE is observed for smaller NWs.<sup>81</sup> The Raman enhancement was attributed to the effects of the resonant cavity and stimulated Raman scattering. In a detailed polarized Raman study of single wurtzite GaN NWs,<sup>36</sup> grown by the VLS process with In as catalyst, Raman intensities of the observed modes as a function of the angle between the long axis of the NW and the electric vector of the incident (and scattered) light was used to distinguish crystalline orientation of the NWs. The role of YL band in the PL spectra and the resonance enhancement of the Raman spectra even with sub-bandgap excitation was believed to be the reason for the complex-valued Raman tensor in single GaN NWs. The authors overlooked the

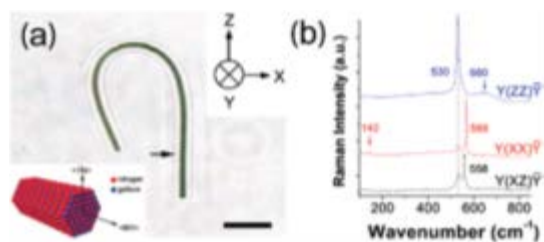


**Figure 16.** (a) Image and polarization configuration of the Raman instrument. The Y direction is labeled for the incoming laser where Z and X define polarizations parallel and perpendicular to the wire growth direction, respectively. Scale bar = 5  $\mu\text{m}$ . Inset: Illustration of crystallographic directions in wurtzite GaN lattice. (b) Polarized Raman spectra of the GaN NW in the  $Y(ZZ)\bar{Y}$ ,  $Y(XX)\bar{Y}$  and  $Y(XZ)\bar{Y}$  polarization configurations. The term  $Y(XZ)\bar{Y}$  indicates the incoming laser approaches from the Y direction and is polarized in X, while signal is collected with Z polarization in the opposite Y direction. The arrow in (a) indicates the area where the spectra shown in (b) have been recorded. (Reprinted with permission from Ref. 37, Copyright © 2005 American Chemical Society)

antenna effect in their study as reported in the previous study of single AlN NR.<sup>81</sup> However, in a seminal paper<sup>37</sup> orientation of [1-100]  $m$ -plane facet of a single GaN NW was uniquely portrayed using polarized Raman study (Figure 16) in  $Y(ZZ)\bar{Y}$  and  $Y(XX)\bar{Y}$  configurations. According to the notation, Z and X are in the plane of the substrate where the nanowire is laid, and the observation is made in the vertical, Y direction. Portion of the 90° bent NW was observed for an intensity imaging in the polarized measurements conforming the orthogonality condition under different polarization condition and corresponding allowed Raman modes in the range below 552  $\text{cm}^{-1}$  and above 558  $\text{cm}^{-1}$ . The study exploited the allowed  $A_1(\text{TO})$  mode at 533  $\text{cm}^{-1}$  and  $E_2(\text{high})$  mode at 567  $\text{cm}^{-1}$  in the respective  $Y(ZZ)\bar{Y}$  and  $Y(XX)\bar{Y}$  configurations for the wurtzite GaN phase to image the nanowire at a different position of the 90° bent. However, the most interesting report<sup>38</sup> was the study of the crystalline orientations of a square faceted GaN nanotube and its sidewall grown in the quasi-VS process by analysing  $E_2(\text{high})/A_1(\text{LO})$  intensity ratios for both  $Z(XX)\bar{Z}$  and  $Z(XY)\bar{Z}$  configurations (panel A Figure 17). A growth mechanism was also proposed for [0001] oriented facets, with minimum free energy of formation, in the square shaped nanotubes.<sup>38</sup> While describing the process of identifying the orientation of the crystalline facets, in a non-destructive polarized Raman study, the authors also emphasized the role of polarization leaking in the nanostructures for the optical measurements in the

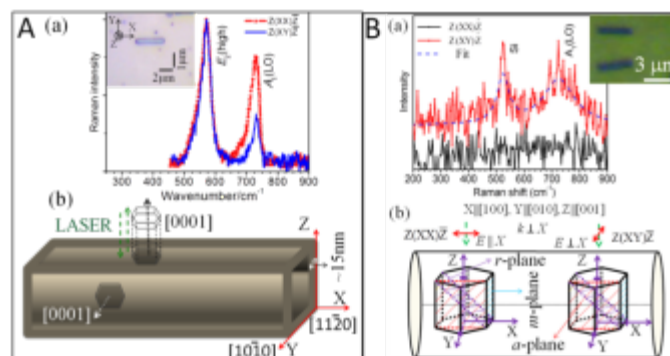


**Figure 17A.** (a) Polarized Raman spectra from a single GaN nanotube collected in parallel  $Z(XX)\bar{Z}$  and perpendicular  $Z(XY)\bar{Z}$  configurations with respect to the nanotube long axis, in backscattering configuration. Nanotube long axis is along X-axis, and incident and scattered light are along Z-axis. Inset, an optical image of a GaN nanotube with laboratory axes. (b) Schematic of square-shaped GaN nanotube with the coordinate axes. All facets of the nanotube tube are having crystallographic orientations along [0001] and nanotube long axis is oriented along [11-20]. Incident and scattered LASER beam (dashed arrowed lines) in the backscattering mode from top facet of nanotube are parallel to Z-axis. (Reprinted with permission from Ref. 38, Copyright © 2013 John Wiley & Sons, Ltd.) B. (a) Polarized Raman spectra for single NW with an excitation wavelength 325 nm for two different polarization configurations  $Z(XX)\bar{Z}$  and  $Z(XY)\bar{Z}$ . The first configuration shows  $A_1(\text{LO})$  mode along with the Si peak but the second configuration shows none of them. The AlGaIn nanowire used for the Raman measurement is shown in the outset. (b) The schematic depiction for single NW with two different polarization configurations used for the polarization study and the possible stacking arrangement of unit cells in the cylindrically shaped NW. (Reprinted with permission from Ref. 83, Copyright © 2015 American Institute of Physics)

diffraction limit. Polarized resonance Raman spectroscopic (RRS) studies were reported (panel B Figure 17) in an optically confined sub-diffraction limited AlGaIn nanowire of diameter  $\sim 100$  nm grown in the single-prong mechanism using VLS assisted CVD technique.<sup>82,83</sup> A monochromatic light source ( $\lambda$ ) of 325 nm with a near ultraviolet (NUV) objective lens of 40X having numerical aperture (N.A.) of 0.50 was used. As per the Abbe diffraction limit ( $\lambda/2N.A.$ ), it is not possible to focus an object below  $\sim 325$  nm. Enhanced light-matter interaction in the optical confinement between semiconducting and dielectric media along with strong electron-phonon coupling in the polarized RRS was proposed to understand the crystallographic orientations in the sub-diffraction length scale. The LO phonon-plasmon coupled mode was attributed to the spontaneous accumulation of electrons on the lateral surfaces of the InN nanocolumns irrespective of its polarity.<sup>84</sup> The surface accumulation of electron was attributed to the In-rich surface reconstruction on the nanocolumn sidewalls during the growth process with varying temperature. The detailed vibrational properties of NWs and NW heterostructures were well reviewed recently.<sup>85</sup> Lattice vibrational properties are proved to be the finger prints for not only the analysis of composition and phase distribution but also the crystalline orientations in single III-nitride nanostructures.

## NANOWIRE PHOTODETECTOR

### High Responsivity and Photoconductive Gain in GaN Nanowires

Ultrahigh photocurrent responsivity ( $R = i_p/P$ ; where  $i_p$  is photocurrent and  $P$  is power of the light source) and photoconductive gain ( $\Gamma = RE/e\eta$ ; where  $e$  is the electron charge,  $E$  is the photon energy, and  $\eta$  is the quantum efficiency of photon absorption) for the UV irradiation has been reported in the catalyst assisted CVD-grown and catalyst free MBE-grown in single GaN NWs.<sup>86,87</sup> The CVD-grown  $m$ -axial single GaN NWs have shown gain values at  $5.0 \times 10^4$ – $1.9 \times 10^5$  for the diameter range of 40 to

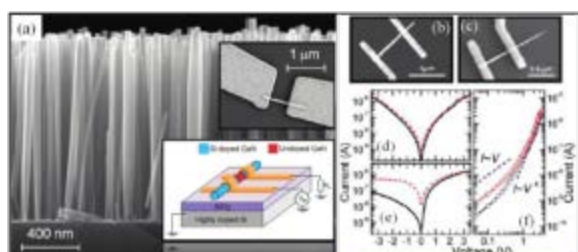


**Figure 18.** (a) Side-view SEM image of  $n$ - $i$ - $n$  GaN NWs on Si(111) substrate. Inset: Top panel is the top-view SEM image of a contacted single NW; bottom panel shows the measurement scheme for characterization of a single NW device. Top-view SEM images and  $I$ - $V$  characteristics at room temperature of single NWs (b,d) with symmetrical contacts on the  $n$ -type regions of the wire and (c,e) with a misalignment leading to one of the contacts touching the undoped region. Solid lines correspond to the dark current; red dashed lines correspond to illumination with  $\sim 0.2$  W/cm<sup>2</sup> of UV light ( $\lambda = 244$  nm). (f) Double logarithmic plot of the  $I$ - $V$  characteristics of a symmetric NW measured in the dark and under UV illumination. For comparison,  $I \sim V$  and  $I \sim V^4$  behaviors are given in dashed lines and solid lines are for eye-guide. (Reprinted with permission from Ref. 87, Copyright © 2012 American Chemical Society)

135 nm.<sup>86</sup> The efficiency ( $\eta$ ) of photon absorption to create electron-hole pairs for the same diameter range is reported to be 26–59 % at 4 eV. The MBE grown  $c$ -axis oriented Si doped single  $n$ - $i$ - $n$  GaN NWs are reported to show the  $\Gamma$  values  $10^5$ – $10^8$  for the diameter range of 50–80 nm (Figure 18).<sup>87</sup> The  $\Gamma$  values of both CVD and MBE-grown GaN NWs are observed to depend on the intensity of the incident photons.

Ultrahigh photocurrent responsivity to UV irradiation has also been reported<sup>43</sup> in the CVD-grown aligned GaN NWs designed as nanobridge (NB) devices (Figure 19). GaN NWs were laterally grown as bridges suspended over the trench between two  $n^+$ -doped GaN electrode posts. The responsivity,  $R$  of the NB device was observed in the range of  $10^4$  to  $10^6$  A/W, which is nearly three to six orders of magnitude higher than the corresponding values (1–3000 A/W) for the photoconductive thin film detectors of GaN. The excess carrier lifetime ( $\tau$ ) in GaN NW ( $\tau = 400$  ms) photoconductor was also observed to be three to seven orders of magnitude higher than the values derived from the thin film photoconductors ( $\tau = 50$  ns–360  $\mu$ s).<sup>88</sup> The device endowed with a large surface area, and a short transport path leads to high responsivity for advanced sensor and detector applications. Although, the presence of minority carrier hole traps, that prolong the lifetime of excess electrons to contribute high gain, has been observed in GaN films, the observed intensity dependent behavior of  $R$  &  $\Gamma$  in GaN NWs suggested a nontrap-dominant mechanism in the NWs. The efficient photo conductivities in single crystalline

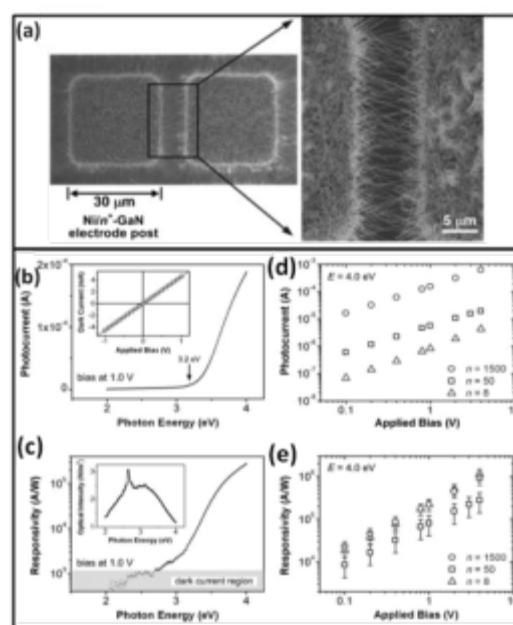


**Figure 19.** (a) Top-view FESEM images of a GaN NB device focused on one pair of Ni/ $n^+$ -GaN electrode posts (left) and on the trench with NWs bridging between two posts (right). (b) Typical photocurrent spectrum and (c) the corresponding responsivity spectrum of the GaN NB device with bridge number 1500 at a bias of 1.0 V. Inset in (b): dark current to bias measurement of the NB device; inset in (c): light source intensity spectrum used for PC characterization. (d) Photocurrent, and (e) responsivity versus applied bias for three GaN NB devices with different bridge numbers  $n$  under excitation at 4.0 eV. (Reprinted with permission from Ref. 43, Copyright © 2008 Wiley-VCH Verlag GmbH & Co.)

GaN NWs prepared by either CVD or MBE have been proposed to be originated from the electron-hole spatial separation induced by SBB. The spatially separated transport of electron-hole ( $e-h$ ) pair prolongs  $\tau$  and thus enhances the  $I$ .<sup>89</sup>

### Size Dependent Photoconduction and Persistent Photoconductivity in Nanowires

The size dependent photoconduction has been observed in both MBE and CVD-grown GaN NWs.<sup>40,41</sup> The size dependence is understood by the model of  $e-h$  spatial separation induced by SBB, as  $\tau$  of the GaN NW is controlled by SBB (Figure 20).<sup>40,89,90</sup> In a recent report, the dependence of SBB on NW diameter and the impurity concentration in GaN NWs was experimentally studied by scanning Kelvin probe microscopy.<sup>91</sup> In the size dependent photoconduction, a critical diameter ( $d_{\text{crit}}$ ) below which a sharp decrease in the photocurrent of the NWs was identified.<sup>40,41</sup> The  $d_{\text{crit}}$  for the MBE-grown GaN NWs was identified as around  $90 \pm 10$  nm, however, for CVD-grown NWs  $d_{\text{crit}}$  is around  $35 \pm 5$  nm. The value of  $d_{\text{crit}}$  is actually determined by the maximal depletion width ( $w$ ) at the surface, *i.e.*,  $d_{\text{crit}} = 2w$ ; where the  $w$  is proportional to  $n_e^{-1/2}$  and  $n_e$  being carrier density. Furthermore, besides the  $n_e$ , the surface polarity of the NW's sidewalls could play a role in the  $d_{\text{crit}}$  as the long-axes of the NWs are different in the two growth methods. A detailed study of comparison of the photoconducting properties of the GaN NWs grown by MBE and CVD techniques have been reported.<sup>89,92</sup>

Measurement of PPC is essential in applications of photodetectors, diode lasers and modulators for high-speed optical data communication; the device must relax quickly to the dark state immediately after the photoexcitation source is off. Native defects, impurities, and surface states together may act as trapping states leading to the observation of PPC in the VLS assisted CVD grown single GaN NWs (Figure 21) connected using FIB assisted electrode formation.<sup>39</sup> Role of the surface space charge region on NWs having different diameters was resolved nicely for diameter dependent PPC studies in MBE grown GaN NWs.<sup>40</sup> The role of SBB was elaborated in an exclusive report of size dependent PPC studies for  $m$ -axial GaN NWs.<sup>41</sup> The temperature-dependent decay time measurements showed effective barrier heights of 226 and 32 meV for 65 and 20 nm NWs, respectively, indicating size dependent SBB effects playing a crucial role in the PPC measurements. Moreover, size-dependent photocurrent decay time reveal that the decay time of the NW above a critical diameter of 30–40 nm was found to be an order of magnitude higher than the smaller NWs. The authors proposed that the surface-induced effective barrier height for different sizes of GaN NWs was the dominant factor in explaining the apparent size dependence.<sup>41</sup>

Back-gated field effect transistors (FETs) made with MBE grown Si-doped polar  $n$ -GaN NWs (Figs. 22(a,b)) were not recommended to be a reliable means of estimating transport parameters because of a long term current drift originating from the injected positive charges screening the back gate.<sup>93</sup> The gate charging effects can be exploited to recuperate from long recovery time of NW based photodetectors. Photoconductivity measurements at 325 nm were used to estimate the drift mobility, and negative surface charge density under vacuum (Figs. 22(c,d)).

Comparative drift effects for both back-gated NW FETs and top-gated NW MESFETs were also studied in different environments of vacuum and air with controlled humidity.<sup>93</sup>

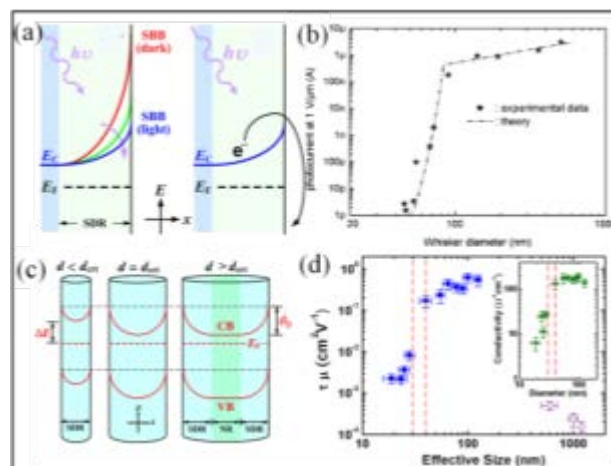


**Figure 20.** (a) Schematic illustration of the decrease of surface band bending (SBB) in the surface depletion region (SDR) by light illumination due to the photovoltaic effect (left) and the mechanism of electron to overcome potential barrier under light illumination to recombine with hole or surface states by thermionic emission (right). (b) The diameter-dependent photocurrent measured under  $15 \text{ Wcm}^{-2}$  UV light intensity of the GaN NWs grown by MBE. [Reprinted with permission from Ref. 40, Copyright © 2005 American Chemical Society] (c) The schematic of real-space energy band diagrams for the NWs with different diameters  $d$ , where the  $\phi_b$  is the maximal barrier height of SBB,  $\Delta E$  is the energy difference between Fermi level and conduction band minimum. (d) The calculated product of carrier lifetime and mobility ( $\tau\mu$ ) of individual NW (solid purple circles) and thin films (open purple diamonds). Inset: The dark conductivity as a function of diameter for NWs in the diameter range of 20 to 126 nm. [Reprinted with permission from Ref. 90, Copyright © 2009 American Institute of Physics]

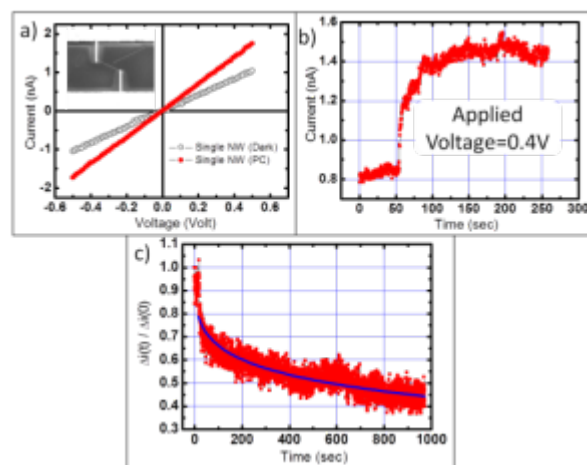


**Figure 21.** Photoconductivity (PC) measurements in (a)  $I$ - $V$  characterization of a single NW in the dark condition and 325 nm laser exposure. (b) Time-dependent PC measurements in a nanowelded NW system typically formed with a fluence of  $5 \times 10^{15}$  ions  $\text{cm}^{-2}$  measure at an applied voltage of 0.4 V. (c) Persistent PC for the same nanowelded NWs. (Reprinted with permission from Ref. 39, Copyright © 2010 American Chemical Society)

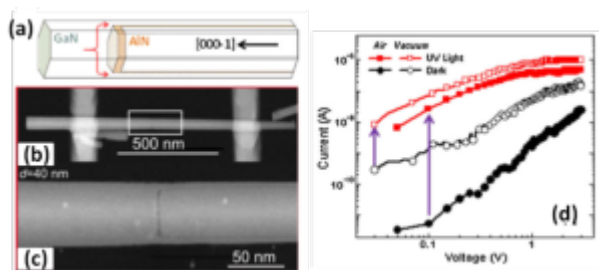


**Figure 22.** (a) Schematic description of the sensor design consisting of a GaN NW with an AlN axial insertion. The lateral growth during the deposition of the AlN and top GaN sections results in the formation of an GaN/AlN/GaN core-shell structure in the base of the wire. The current flow (red arrows) is drifted towards the NW surface. (b) STEM image of a contacted NW and (c) magnified image of the AlN insertion. The AlN shell is visible in the image with a darker contrast. (d) Variation of the dark current and photocurrent as a function of the measurement atmosphere. The photocurrent is excited by illumination with  $\sim 0.2 \text{ W/cm}^2$  of UV light ( $\lambda=244 \text{ nm}$ ). (Reprinted with permission from Ref. 44, Copyright © 2013 Institute of Physics)

### Single Nanowire Photodetector

A wider range of absorption wavelength, a several-fold increase in the dipole matrix element, and higher absorption probability for nonpolar III-nitride based QW structures than those for a polar variant of it was predicted due to the absence of polarization-related electric fields in the former.<sup>94</sup> PA-MBE grown undoped single GaN NWs showed a dark current three-orders of magnitude lower and a photocurrent gain of about one-order of magnitude higher with respect to those for  $n-i-n$  single NWs based photodetectors where  $n$ -GaN was achieved using Si as dopant.<sup>44</sup> Accomplishment of the single GaN/AlN/GaN core-shell NWs as photodetectors was reported with photocurrent gain in the range of  $10^5$ – $10^8$ , and a UV to visible contrast ratio  $>10^6$  (Figure 23). The single-wire photodetectors using  $n-i-n$  MQW junctions of nonpolar  $[\text{In}_{0.16}\text{Ga}_{0.84}\text{N}/\text{GaN}]_5$  undoped radial QWs ( $i$ -layer),

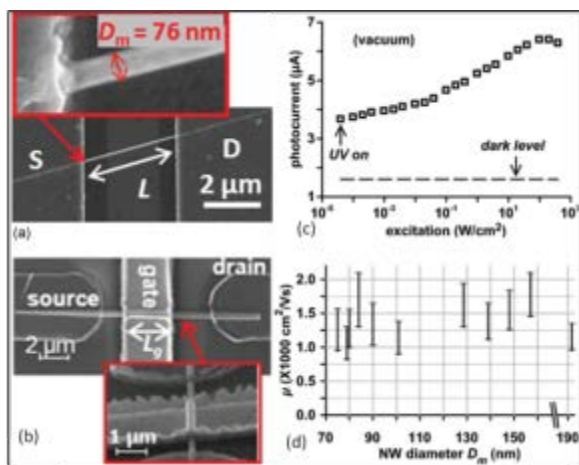


**Figure 23.** (a) FESEM image of sample 2 illustrating typical back gated FET configuration. (b) Image of typical MESFET sample. (c) Photocurrent  $I_{sd}^p$  recorded under vacuum on sample 15 for  $V_{sd} = 20 \text{ mV}$  and  $40 \mu\text{W cm}^{-2} < P_{325}^{325} < 390 \text{ W cm}^{-2}$ . The dark level prior to any UV excitation is also shown. (d) Extremal values  $\mu^\pm$  calculated from saturated photocurrent  $I_{sd}^p$  as described in the text. (Reprinted with permission from Ref. 93, Copyright © 2013 American Institute of Physics)

grown using catalyst free MOVPE (Figs. 24(a-c)), were found to be sensitive to energy  $>2.6 \text{ eV}$  with a high photoconductive gain of  $2 \times 10^3$ .<sup>45</sup> The scanning photocurrent microscopy (SPCM) maps confirmed that the detector response was in the  $n-i-n$  junction, which was localized at the edge of NW containing the QWs for both below and above GaN bandgap at 488 and 244 nm, respectively (Figs. 24(d-g)). Photoconductive parameters of different III-nitride NWs are tabulated (Table 1).

Joule self-heating and high photocurrent were thought to be an important performance parameter for NW based photodetectors in the perspective of operational reliability.<sup>95</sup> Thermal transport and effect of Joule-heating in GaN NWs were reported,<sup>46</sup> using a combination of micro-PL and in-situ TEM studies. A very low thermal conductivity  $<80 \text{ W/m-K}$ , substantially lower than the bulk GaN value, leads to a breakdown at  $\sim 1000 \text{ K}$  due to thermal decomposition. Ultrahigh photocurrent gain and fast responses in III-nitride based single nanowire devices make them prominent candidates for on-chip optical detection for a wide range of wavelengths.

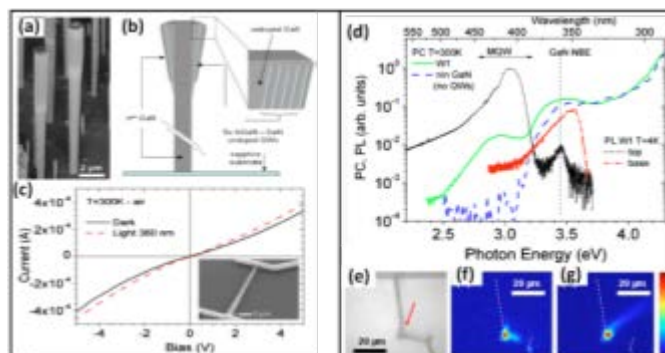


**Figure 24.** (a) SEM image of the as-grown NWs on sapphire substrate; (b) scheme of the heterostructure and of the doping profile; (c)  $I$ - $V$  curves of a single-NW device at RT in air, in the dark (black solid line), and under illumination at  $\lambda=360 \text{ nm}$  and  $P_{\text{inc}}=30 \text{ mW/cm}^2$  (red dashed line). In the inset, SEM image of the corresponding device. The NW length is  $20 \mu\text{m}$ . (d) Normalized PC spectrum of W1 at  $1 \text{ V}$  bias (green solid line) and of a NW from a reference  $n-i-n$  GaN sample without QWs (blue dashed line);  $\mu$ -PL spectra from the top (black dotted line) and from the base (red dash-dotted line) of W1; all spectra have been collected at RT in air. (e) UV micrograph visualizing the area containing the contacted W1 analyzed by means of SPCM. The red arrow points to the NW top. [(f) and (g)] SPCM images collected exciting the sample with laser light at (f)  $\lambda=488 \text{ nm}$  and (g)  $\lambda=244 \text{ nm}$ . The scale reported on the right-hand side is linear from 0 to the maximum PC recorded within each image. (Reprinted with permission from Ref. 45, Copyright © 2011 American Institute of Physics)

### Nanowires for Coupling of Light and Use as Detectors

Intrachip optical interconnects using nano-devices is proposed with the advantages of increased bandwidth, free of electromagnetic interference, and voltage isolation over interconnected electrical devices. It is ultimate to design an optical source, and a detector integrated on-chip paving the path for an all-optical device for the future. Optical coupling of two single NW based devices, comprising of axial  $p-n$  junction GaN NWs (Figure 25) working as LED and an  $n$ -GaN based photoconductive

**Table 1:** Comparison of photoconductive parameters of different III-nitride NWs.

Growth strategy; Type of NWs	Single /Ensemble	Size (nm)	Photo current (A)	Photo Current Gain	Responsivity (A/W)	Refs.
MBE; GaN	Single	>100, <100	$10^{-6}$ - $10^{-5}$ , $10^{-12}$ - $10^{-6}$ @ 150 KW/m <sup>2</sup> & 1 V/ $\mu$ m	---	---	40
CVD; GaN	single	20-60	$10^{-6}$ - $10^{-5}$ @ 1 V &	$\sim 10^2$ @ 1W/m <sup>2</sup>	---	41
CVD; GaN	Ensemble	20-60	$10^{-6}$ - $10^{-4}$ @ 1 V	---	$\sim 10^4$ - $10^6$ @ 4 eV	43
MBE; GaN/AlN	Single	$\sim 50$	$\sim 10^{-8}$ @ 3 V	$\sim 10^5$ - $10^8$ @ 2 W/m <sup>2</sup>	---	44
MOVPE; InGaN/GaN	Single	>500	$10^{-5}$ @ 5 V	$\sim 10^3$ @ 300 W/m <sup>2</sup>	$\sim 10^4$ @ 3.1-3.4 eV	45
MBE; GaN	Single	---	$10^{-7}$ @ 10V, 10W/m <sup>2</sup>	---	---	47
MOVPE; InGaN/GaN	Single	>700	---	---	$\sim 10^4$ @ 3.1-3.4 eV	48
CVD; GaN		40-150	$10^{-7}$ @ 0.1V	$\sim 10^4$ - $10^5$ @ 10W/m <sup>2</sup>	---	86
MBE; GaN	Single	50-80	$10^{-8}$ - $10^{-7}$ @ 1V	$\sim 10^5$ - $10^8$ @ 2KW/m <sup>2</sup>	---	87
CVD; GaN	Single	65-100	$10^{-7}$	$\sim 10^3$ - $10^5$	---	89, 92
MBE; GaN	Single		$10^{-8}$ @ 1V	$\sim 10^3$ - $10^4$ @ 1-10 <sup>2</sup> W/m <sup>2</sup>	---	
MBE; GaN	Single	---	$10^{-6}$ @ 0.2 V	---	---	93

receptor, was realized recently for the first time.<sup>47</sup> The optical coupling demonstrated in this device may provide new opportunities for integration of optical interconnects between on-chip electrical subsystems. With a further stretch of imagination, on-chip fabrication of nano-phonic devices consisting of single wire LED and photodetectors optically coupled by waveguides was demonstrated.<sup>47</sup> Core-shell *p*-InGaN/*n*-GaN NWs on Si/SiO<sub>2</sub> templates and connected by  $\sim 100 \mu\text{m}$  long nonrectilinear SiN waveguides were used for realizing these devices with a communication wavelength of 400 nm (Figure 26). A fast transition time below 0.5 s was reported for the LED on/off

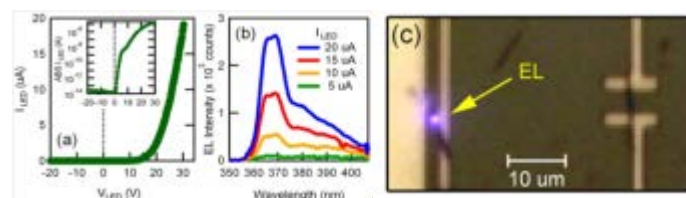


**Figure 25.** LED NW characteristics: (a) I–V characteristics, (b) electroluminescence spectra, and (c) image of electroluminescence (EL) emission. (Reprinted with permission from Ref. 47, Copyright © 2013 American Chemical Society)

switching and photodetector current variation with it.<sup>48</sup> Light emission and detection by single nanowire devices based on III-nitride nanostructures demonstrate first experimental evidence of all optical devices in electronic processing, which may increase the speed of the electronic devices by many folds.

## PHOTOELECTROCHEMICAL PROPERTIES AND ARTIFICIAL PHOTOSYNTHESIS

### Cocatalyst Decoration and Bandgap Engineering of III-Nitride Nanowires

A schematic view of the PEC process of water splitting under light illumination is depicted in Figure 27. The use of solar energy in generating H<sub>2</sub> from water splitting process is one of the important sustainable technologies for a renewable source of clean and storable energy. Thus, the development of efficient photoelectrode material sensitive to the major part of the solar spectrum, including visible light, has been of immense significance. The photocatalytic activity for water splitting by cocatalytic Rh/Cr<sub>2</sub>O<sub>3</sub> core-shell nanoparticles decorated MBE grown GaN NWs photo-electrode was reported.<sup>96</sup> The H<sub>2</sub> evolution was promoted by the Rh noble metal core with the

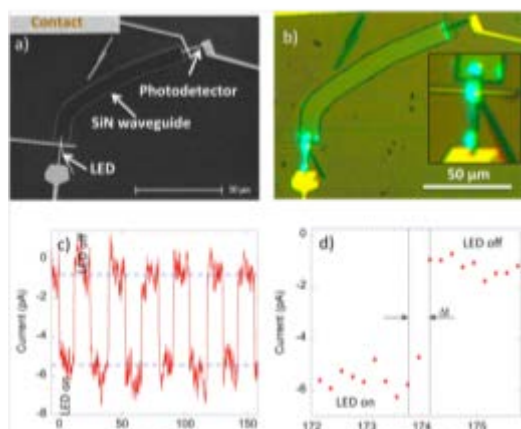


**Figure 26.** (a) SEM image of a detector/emitter couple. (b) Optical microscope image of the detector/emitter couple under operation. The inset to (b) shows a close-up on the LED. (It should be noted that the microscope camera filter changes the color rendering toward green tone). (c) Current temporal trace of the detector when the LED is repeatedly switched on and off. (d) Detail of current variation between on and off states. (Reprinted with permission from Ref. 48, Copyright © 2014 American Chemical Society)

exposure of Xe lamp. At the same time the  $\text{Cr}_2\text{O}_3$  shell, acting as an  $\text{O}_2$  diffusion barrier, prevented water formation in the back reaction over Rh (Figure 28). A highly stable photocatalytic process was established for the decomposition of pure water by GaN NWs electrode, with the higher turnover number per unit time than that reported for GaN powder samples.<sup>97</sup> Multiple QD and QW heterostructures of InGaN/GaN NWs grown with the RF PA-MBE technique, decorated with Rh/ $\text{Cr}_2\text{O}_3$  core-shell nanoparticles was shown (Figure 29) by the same group to produce  $\text{H}_2$  using pure water (pH ~ 7.0) under UV-Vis light up to ~560 nm, which was the longest wavelength ever reported for this purpose.<sup>98</sup> The stable photocatalytic activity of the NW heterostructures with the highest internal quantum efficiency of ~13% at 440-450 nm was recorded in the visible spectrum with a high turnover number.

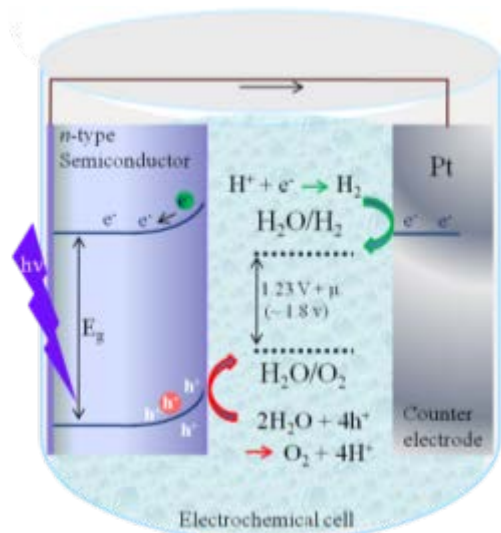


**Figure 27.** Schematic view for the PEC process of water splitting under light illumination.

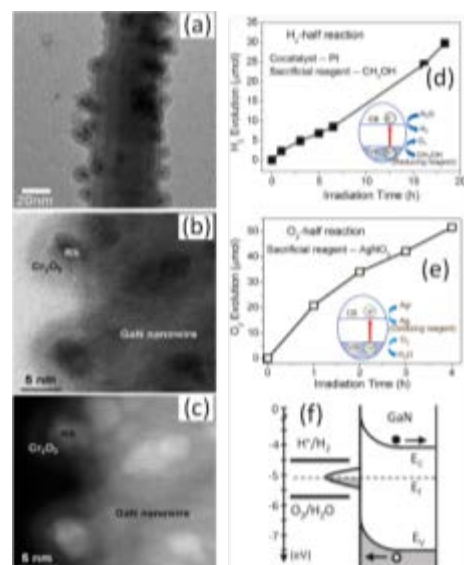


**Figure 28.** (a) Low magnification TEM image shows uniform distribution of the Rh/ $\text{Cr}_2\text{O}_3$  nanoparticles on GaN NW surfaces. (b) HRTEM image and (c) HR-HAADF image clearly show the Rh/ $\text{Cr}_2\text{O}_3$  core-shell nanostructures deposited on GaN NWs. (d)  $\text{H}_2$  and (e)  $\text{O}_2$  evolution half-reactions in the presence of respective sacrificial reagents over GaN NWs under a 300W full arc xenon lamp irradiation. The corresponding reaction processes are schematically illustrated in the insets. (f) GaN surface defects pin the Fermi level at the surface and bend the bands upward, thereby driving holes to the NW sidewall and electrons into the bulk. (Reprinted with permission from Ref. 96, Copyright © 2011 American Chemical Society)

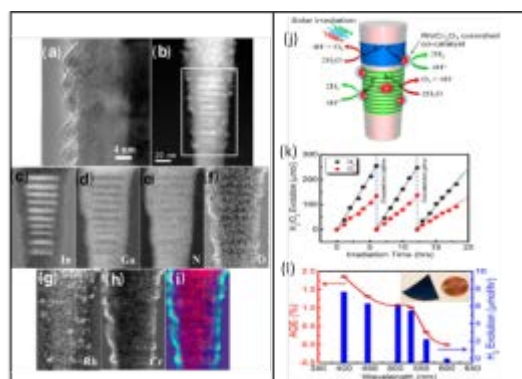


**Figure 29.** TEM characterization of Rh/ $\text{Cr}_2\text{O}_3$  decorated InGaN/GaN NWs. (a) High resolution TEM of Rh/ $\text{Cr}_2\text{O}_3$  nanoparticles on the lateral surfaces of NW. (b) Electron energy loss spectroscopy (EELS) spectrum image of Rh/ $\text{Cr}_2\text{O}_3$  deposited InGaN/GaN NW. (c-h) Elemental maps of the nanoparticle deposited InGaN/GaN NW, derived from the selected area in EELS spectrum image (b) with MLLS fitting. (i) RGB elemental mixing (red, Rh; green, Cr; blue, O) image showing the core-shell Rh/ $\text{Cr}_2\text{O}_3$ . Overall water splitting and apparent quantum efficiency. (j) Schematic of the photocatalytic overall water splitting reaction mechanism. (k) Overall pure water splitting on Rh/ $\text{Cr}_2\text{O}_3$  decorated InGaN/GaN NW arrays under full arc (>300 nm) 300 W xenon lamp irradiation. (l) Apparent quantum efficiency (AQE) (red line and solid square symbol, left axis) and  $\text{H}_2$  evolution rate (blue columns, right axis) as a function of wavelength of the incident light. The horizontal error bars represent the full-width-half maximum of the optical filters. The  $\text{H}_2$  evolution rate was derived from ~2 h of overall water splitting under each optical filter. The solid red line is a guide to the eye. The inset shows a typical NW sample used for overall water splitting. (Reprinted with permission from Ref. 98, Copyright © 2013 American Chemical Society)

The enhanced efficiency of  $H_2$  generation is possible by effectively absorbing photons within a wide range of the solar spectrum. By applying bandgap engineering and geometry optimization, photocurrent density of CVD-grown 3-D hierarchical Si/InGaN NW arrays was enhanced by five times compared to that for InGaN NW arrays on planar Si (Figure 30).<sup>49</sup> Bandgap engineering by In incorporation in the 3D epitaxial GaN-In<sub>x</sub>Ga<sub>1-x</sub>N core-shell rod arrays was further allowed to match the visible absorption with the solar spectrum as well as to align the semiconductor bands close to the water redox potentials to achieve high efficiency for visible light driven water splitting.<sup>99</sup> In fact, CVD-grown GaN NWs as photo-electrode, without any catalyst decoration showed PEC conversion efficiency of 1.09 % in contrast to 0.58 % of GaN thin film counterpart under similar experimental conditions.<sup>100</sup> The efficiency of  $H_2$  generation has been further enhanced by adaptive multijunction photoelectrode architecture by integrating narrow bandgap planar Si solar cell (*n*+*p* Si) wafer at the bottom and wide bandgap *p*-InGaN (600 nm) NWs array grown on *n*-GaN (150 nm) at the top of the photoelectrode.<sup>101</sup> A polarization-enhanced tunnel junction (*n*<sup>++</sup>-GaN (20 nm)/In<sub>0.4</sub>Ga<sub>0.6</sub>N/*p*<sup>++</sup>-GaN(20 nm)) was incorporated between *n*-GaN and *p*-InGaN for the transport of photoexcited holes within every single NW. The architecture of the photoelectrode is enabled to absorb the ultraviolet and a large portion of the visible and infrared solar spectrum (280-1100 nm), thus generating a saturated photocurrent density of -40.6 mA/cm<sup>2</sup> at normal hydrogen electrode potential  $V_{NHE} = 0.26$  V. The photoelectrode also exhibited a maximum applied bias photon-to-current efficiency (ABPE) of 8.7% at  $V_{NHE} = 0.33$  V.<sup>101</sup> These studies establish the use of III-nitride NWs as viable photoelectrodes for the production of  $H_2$  as solar-fuel in the artificial photosynthesis process.

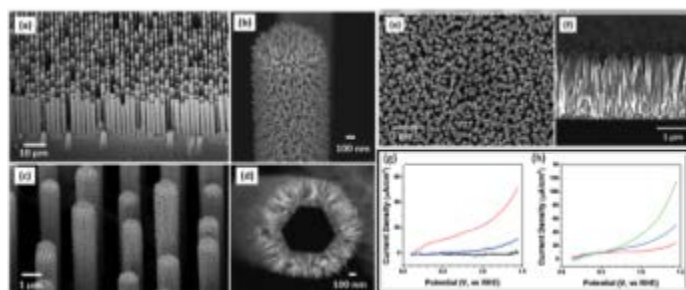


**Figure 30.** Tilted (45°) SEM images of hierarchical Si/In<sub>x</sub>Ga<sub>1-x</sub>N NW arrays on Si(111) substrate with X = 0.08–0.1 (a–c). A fractured wire reveals the cross section (d) showing that InGaN NWs grow vertically from the six Si wire facets. Top down (e) and cross sectional (f) SEM images of vertical In<sub>x</sub>Ga<sub>1-x</sub>N NWs grown on a planar Si(111) substrate. Photoelectrochemical measurements on Si/In<sub>x</sub>Ga<sub>1-x</sub>N (x = 0.08–0.10) photoanodes. Photocurrent density plots (g) of hierarchical Si/In<sub>x</sub>Ga<sub>1-x</sub>N NW arrays (red) and planar Si/In<sub>x</sub>Ga<sub>1-x</sub>N (blue) under 100 mW/cm<sup>2</sup> without AM 1.5 filter show an increase in current for the hierarchical geometry. A representative dark current density plot is shown in black. Photocurrent density plots (h) of hierarchical Si/In<sub>x</sub>Ga<sub>1-x</sub>N NW arrays show a photocurrent dependence on illumination condition: red (100 mW/cm<sup>2</sup> with AM 1.5 filter), blue (100 mW/cm<sup>2</sup> without AM 1.5 filter), and green (350 mW/cm<sup>2</sup> without AM 1.5 filter). (Reprinted with permission from Ref. 49, Copyright © 2012 American Chemical Society)

### Role of Doping in Nanowire Photo-Electrodes

The dark conductivity of GaN NWs photo-electrode can be controlled by doping and external bias.<sup>102</sup> By applying an external bias the electrochemical properties of the photo-electrode can be modified due to the variations in SBB. In this context, a detailed study has been conducted and analyzed the electrochemical properties (surface capacitance ( $C_s$ ) and surface resistance ( $R_s$ ) at the NW/electrolyte interface) of non-intentionally doped, Si-doped, and Mg-doped GaN NWs grown on highly conductive Si(111) substrates.<sup>102</sup> Increase of the Si concentration in GaN NWs leads to an increase of  $C_s$  and a simultaneous decrease of  $R_s$  (conductive NWs). Whereas non-intentionally doped NWs, Mg-doped, and moderately Si-doped GaN NWs (resistive) showed low  $C_s$  and high  $R_s$  values. The photoelectrochemical properties of both undoped and Si-doped *n*-GaN NW arrays were reported using HBr and KBr electrolytes.<sup>50</sup> The role of SBB on GaN and its variation with the dopant incorporation were studied in the context of photocurrent generation with the variation of bias voltage. Maximum efficiencies of ~15 and 18% were measured at 350 nm light illumination for undoped and *n*-GaN NWs, respectively. Hydrogen generation on a double-band photoanode of MBE grown *n*-type InGaN/GaN core/shell NW arrays on Si substrate in an acidic solution of HBr was reported.<sup>51</sup> The *n*-type NWs were used to reduce the surface depletion region and increase the current conduction. The high conversion efficiency of ~27% was measured under UV-Vis light irradiation along with a steady evolution of  $H_2$  under a solar simulator. Surface charge properties of Mg-doped *p*-GaN and Si-doped *n*-GaN were reported in a recent article.<sup>102</sup> Based on this result, surface charge properties of *p*-GaN NWs were controlled by tuning the surface Fermi level to overcome the major impediments for achieving very efficient and extremely stable overall water splitting over the emerging nanoelectrode based photocatalyst in a seminal report.<sup>57</sup> The internal quantum efficiency and activity on *p*-GaN NWs were reported ~51% and ~4.0 mol hydrogen h<sup>-1</sup>·g<sup>-1</sup>, respectively. The nanoelectrodes were decorated with Rh/Cr<sub>2</sub>O<sub>3</sub> core-shell nanoparticles for utilizing the catalytic activity also in achieving such an

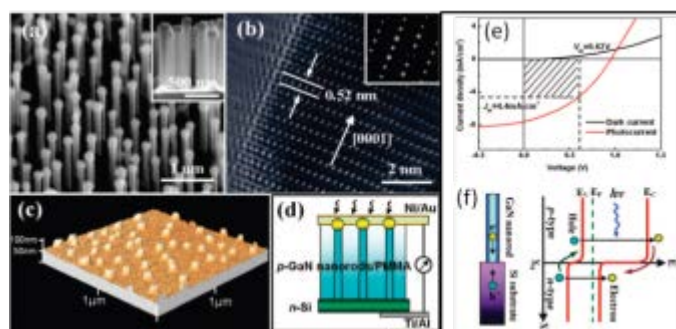


**Figure 31.** (a) Tilt top view SEM image of Mg-doped GaN nanorod arrays. Inset shows cross-sectional SEM image. (b) HRTEM image of GaN nanorod and its corresponding SAED pattern (inset). (c) AFM image of GaN nanorod tips exposed above the photoresist layer. (d) A schematic of the *p*-GaN nanorod/*n*-Si heterojunction photovoltaic cell. (e) Current density vs voltage for the solar cell in the dark and under simulated AM1.5G illumination with an intensity of 100 mW/cm<sup>2</sup>. (f) Schematic energy band diagram of the heterojunction diode showing the photogenerated carrier transfer process. (Reprinted with permission from Ref. 61, Copyright © 2008 ACS)

**Table 2:** Comparison of photoelectrochemical parameters of different III-nitride NWs.

Growth strategy; Type of NWs	Size (nm)	Electrolytes	Reference & Counter electrodes	Photocurrent densities (mA/cm <sup>2</sup> )	Incident- photon-to- current- conversion efficiency (IPCE) (%)	H <sub>2</sub> Generation rate (μmol h <sup>-1</sup> )	Refs.
PECVD; Si/InGaN Core/Shell	~ 700/ <100	H <sub>2</sub> SO <sub>4</sub> + Na <sub>2</sub> SO <sub>4</sub>	Ag/AgCl & Pt mesh	0.062 @ 1.23 V & 350mW/cm <sup>2</sup>	---	---	49
MBE; GaN a) Undoped b) Si doped	30-110	HBr	Ag/AgCl & Pt wire	a) 10 b) 14 @ 1V & 13.2mW/cm <sup>2</sup>	a) 18 b) 15	a) ~38 b) ---	50
MBE; InGaN/GaN core/shell	80-140	HBr	Ag/AgCl & Pt	23 @ 1V	27.6	~10	51
MBE; GaN a) <i>n</i> -type b) <i>p</i> -type	50-75	CH <sub>3</sub> OH in H <sub>2</sub> O with Rh catalyst	---	---	---	a) ~ 45 b) ~ 10	a) <sup>57</sup> b) <sup>96</sup>
MBE; InGaN/GaN	30-70	CH <sub>3</sub> OH in H <sub>2</sub> O	---	---	---	a) 3 (With Pt catalyst) b) 38 (Rh/Cr <sub>2</sub> O <sub>3</sub> )	98
MOVPE; GaN-InGaN core-shell	~900	H <sub>2</sub> SO <sub>4</sub>	---	0.3 mA/ @ 1.3 V & 100mW/cm <sup>2</sup>	---	---	99
CVD; GaN	>50 nm	HCl	Ag/AgCl & Pt	0.8 @ 0.3V & 100mW/cm <sup>2</sup>	1.09	---	100
MBE; <i>p</i> -InGaN/tunnel junctions/ <i>n</i> -GaN	50-150	HBr	Ag/AgCl & Pt	-40.6 @ 0.3V & 130mW/cm <sup>2</sup>	72.3	130	101

encouraging value. The study showed the essential role of Fermi-level tuning in balancing redox reactions and in enhancing the efficiency and stability of the photo-electrode. Doping played a crucial role in enhancing the hydrogen generation by III-nitride nanostructures as photo-electrodes. Comparison of photoelectrochemical parameters of different III-nitride NWs is tabulated (Table 2).

### PHOTOVOLTAIC CELL USING 1-D III-NITRIDE NANOSTRUCTURES

An array of aligned 1-D III-nitride nanostructures are prospective building blocks for optoelectronic devices, such as solar cells, providing large surface area and direct conduction paths for photogenerated carriers to transport across the junction and external electrode leading to high carrier collection efficiency. As compared to polycrystalline films, superior carrier diffusion coefficient and electron recombination time of ordered 1-D nanostructures is likely to increase the diffusion length of minority carriers. Moreover, 1-D nanostructure arrays have low optical reflectance over a wide spectral range.<sup>103</sup> Photovoltaic properties of 1-D nanostructure arrays such as TiO<sub>2</sub>,<sup>104</sup> ZnO nanotubes,<sup>105</sup> and Si NWs<sup>106</sup> demonstrated promising device characteristics as compared to the corresponding 2-D film and bulk counterparts.

A vertically aligned photovoltaic cell was prepared by forming *p*-GaN nanorod/*n*-Si heterojunction (Figs. 53(a-d)) in the Au

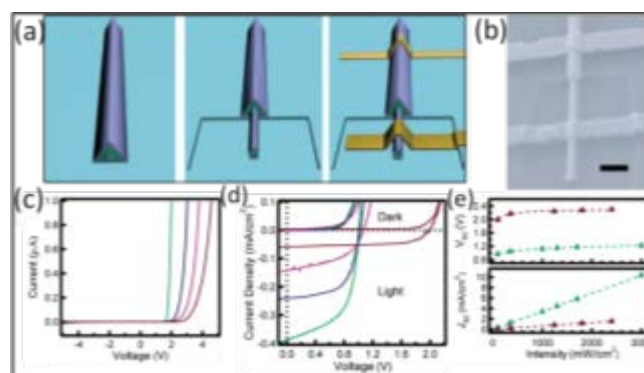


**Figure 32.** Device fabrication and characterizations. (a) Schematics of device fabrication: left, coaxial *n*-GaN/*i*-In<sub>x</sub>Ga<sub>1-x</sub>N/*p*-GaN NW heterostructures; middle, exposed the *n*-core at NW end following ICP-RIE etch; right, Ni/Au and Ti/Al/Ti/Au metal contacts deposited on the *p*-shell and *n*-core, respectively. (b) SEM image of a representative NW device. Scale bar is 2 μm. (c) Dark *I*-*V* curves of three heterojunction NWs (from left to right, denoted with green, blue and purple color with increasing InGaN layer growth temperature 715, 745, and 775 °C) and one homojunction (*x* = 0) NW (denoted with dark violet color). (d) Dark and light *J*-*V* curves of representative ultraviolet, purple, blue, and green nanowire Photovoltaic devices. (e) Light intensity dependent on *J*<sub>sc</sub> and *V*<sub>oc</sub> for representative ultraviolet (dark violet triangles) and green (green triangles) devices. Lines through the *V*<sub>oc</sub> and *J*<sub>sc</sub> data correspond to logarithmic and linear dependencies, respectively. (Reprinted with permission from Ref. 62, Copyright © 2009 American Chemical Society)

**Table 3:** Comparison of photovoltaic parameters of different III-nitride NW devices.

Growth strategy; NWs device structure	Single/ Ensemble	Size (nm)	Short-circuit current density, $J_{sc}$ (mA/cm <sup>2</sup> ) @ 1-sun (AM 1.5G)	Open-circuit voltage $V_{oc}$ (V)	Fill factor (FF)	Maximum Power conversion efficiency ( $\eta$ ) %	Refs.
CVD; <i>p</i> -GaN NWs on <i>n</i> -Si	Ensemble	~100	~7.6 @ 100 mW/cm <sup>2</sup>	~0.95	~0.38	~ 2.73	61
MOCVD; a) <i>n</i> -GaN/ <i>i</i> -In <sub>x</sub> Ga <sub>1-x</sub> N/ <i>p</i> -GaN core/shell/ shell b) <i>n</i> -GaN/ <i>p</i> -GaN	Single	---	a) 0.39  b) 0.059 1.0	a) 1.0  b) 2.0 0.5	a) 0.56  b) --- 0.54	a) 0.19  0.3	62
MOCVD & ICP etching; <i>p</i> -InGaN/ InGaN/InGaN MQW/ <i>n</i> -GaN	Ensemble	~400	1.0	0.5	0.54	0.3	63
MOCVD & ICP etching; <i>p</i> -InGaN/InGaN MQW/ <i>n</i> - GaN a) Nanorods b) Nanoholes	Ensemble	a) 220  b) 220	a) 1.14  b) 1.37	a) 1.9  b) 1.9	a) 0.51  b) 0.5	a) 1.12  b) 1.28	64

catalyst assisted halide CVD technique.<sup>61</sup> The *p-n* junction, with a rectification ratio larger than  $10^4$  in the dark, showed a high short-circuit photocurrent density of  $7.6 \text{ mA}\cdot\text{cm}^{-2}$  and energy conversion efficiency of 2.73% under one sun air-mass 1.5 global spectrum (AM 1.5G) illumination at  $100 \text{ mW}\cdot\text{cm}^{-2}$  (Figs. 31(e,f)). Moreover, the nanorod array may be used as an antireflection coating for solar cell applications. A study on the comparison of photodiode characteristic of single and ensemble *p*-GaN NW/*n*-Si heterojunction devices revealed the role of Mg defect states in the photoresponse under below-bandgap excitation.<sup>107</sup> Photovoltaic mode of the ensemble NW heterojunction device showed an improvement in the fill-factors up to 60% over the single NW device with fill-factors up to 30%. Coaxial group III nitride photovoltaic devices made of a single *n*-GaN/*i*-In<sub>x</sub>Ga<sub>1-x</sub>N/*p*-GaN NW was also realized.<sup>62</sup> Variation of the In mole fraction was used to control the active intrinsic *i*-layer bandgap (556-371 nm) for the light absorption. With the decrease of In composition from 0.27 to 0 an increase in the open-circuit voltages ( $V_{oc}$ ) from 1.0 to 2.0 V and decrease in the short-circuit current densities ( $J_{sc}$ ) from 0.39 to 0.059  $\text{mA}\cdot\text{cm}^{-2}$  was observed for simulated one-sun AM 1.5G illumination (Figure 32). Maximum efficiency of ~0.19% was achieved in this process.<sup>62</sup> The demonstration of single core-shell NWs device is a promising exponent for exploring nanostructure based photovoltaic applications. In another unique effort with similar configuration, a photovoltaic cell consisting of a vertically aligned array of InGaN/GaN MQW core-shell NWs which were electrically connected by a *p*-InGaN cover layer (Figs. 33(a-f)) was demonstrated.<sup>63</sup> The hybrid structure was based on standard planar device processing, while the advantages of 1-D NW, with a strain free light absorbing layer of In rich InGaN layers, efficient carrier collection in thinner layers, and enhanced light trapping from nanoscale optical index changes, were exploited. The cells showed photoresponse up to 2.1 eV,  $J_{sc} \sim 1 \text{ mA}\cdot\text{cm}^{-2}$  and a maximum efficiency ~ 0.3% under 1 sun AM1.5G (Figure 33g). Most recently, photovoltaic cells made of

InGaN/GaN MQW layer in the basic module of *p*-GaN/[InGaN/GaN]<sub>10</sub>/*n*-GaN operating at a wavelength of 520 nm was reported.<sup>64</sup> A periodic nanorod or nanohole array was fabricated on the top *p*-GaN layer by means of modified nanosphere lithography. Under one sun AM1.5G illumination, a fill factor of 50% (0.5), and a  $V_{oc}$  of 1.9 V were achieved with In rich InGaN layers which usually degrades the crystal quality by introducing strain. Nanostructuring of the top *p*-GaN layer significantly improved the photovoltaic cell performance with more than 50% enhancement of the nanohole configuration as compared to the 2-D film. It is too early to make comments, but photovoltaic applications of hetero and homojunction III-nitride nanostructures are promising particularly with the possibility of such wide energy (0.7-6.2 eV) coverage for specific compositions. Comparison of photovoltaic parameters of different III-nitride NW devices are tabulated (Table 3).

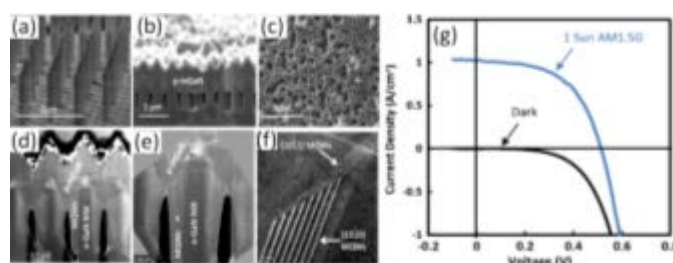


**Figure 33.** Scanning electron microscope images of (a) a representative NW array after dry and wet etching, (b) a tilted cross-section of the completed III-nitride NW structure, and (c) a top-view of the *p*-InGaN layer showing the faceted surface. Scanning transmission electron microscope images of (d) a row of NWs, (e) a single NW, and (f) a close-up of the semi-polar and m-plane MQWs. (g) Current density versus voltage characteristics of the III-nitride NW solar cell under dark and 1 sun (AM1.5G) conditions. (Ref. 63@2012, Copyright © Institute of Physics; Applied for permission)

## CONCLUSIONS

We have tried to assimilate and present important research results of one of the most important class of semiconducting materials of 1-D III-nitride with direct bandgap and high mobility for high speed all-optical device applications. The size and distribution (single or arrayed, aligned or otherwise) effect of these nanostructures on their optical properties is discussed. The role of defects in the luminescence behavior and its influence in the phonon properties are also discussed. Conventionally forbidden surface optical modes (owing to conservation of momentum of the surface atoms) are reported for the 1-D III-nitride nanostructures in the presence of surface irregularities, along with polarized Raman study, to understand the crystalline orientation and antenna effect. Single and multiple quantum well structures are also reviewed for its enormous capabilities in manipulating the luminescence properties of 1-D III-nitride nanostructures. Electroluminescence and light emitting diode properties are also studied in the cases of axial and radial *p-n* junctions of these III-nitride nanostructures. Optically pumped lasing for single wavelength in single GaN NWs and tunable wavelength in 1-D single InGaN/GaN multiple quantum well nanostructures are also described in sufficient details. Performances of 1-D III-nitride NWs as photodetectors are also reviewed for persistence photoconductivity and responsivity along with optical gain as basic detector parameters. As one of the most astounding properties, coupling of optical emission and detection are presented, in case of direct bandgap semiconducting materials. Though the optical coupling of light in III-nitride nanostructure is in its preliminary stage, it is a sensational achievement in the field of all optical communication. In resourcing renewable energy, both photoelectrochemical and photovoltaic properties are reviewed in detail. Generation of hydrogen for the fuel cell application is demonstrated for catalyst assisted and doped 1-D III-nitride nanostructures with the exposure of UV and visible light. Even if it is in its infancy, the role of radial III-nitride nanostructures in solar cell application is promising with the possibility of heterojunctions covering a wide 0.7-6 eV range of the electromagnetic radiation.

The use of the 1-D III-nitride nanostructure in all-optical communication using its capability of efficient tunable emission process and detection of light for a wide range of the electromagnetic spectrum will be detrimental in dominating the semiconducting technology. More studies, in multiple quantum well structures as source of light and detector, are thus welcome. Research on 1-D III-nitride nanostructures is also demanding in resourcing renewable energy either in the fuel cell and solar cell applications.

## ACKNOWLEDGMENTS

Author (AP) acknowledges Department of Atomic Energy for providing financial aid in continuing the research work. Financial support by the Ministry of Science and Technology, Ministry of Education in Taiwan is acknowledged.

## REFERENCES AND NOTES

- U. Woggon. Optical properties of semiconductor quantum dots, Springer-Verlag: Berlin Heidelberg, **1997**, vol, 136.
- M. Mikkelsen, J. Berezovsky, N. Stoltz, L. Coldren, D. Awschalom. Optically detected coherent spin dynamics of a single electron in a quantum dot. *Nat. Phys.* **2007**, 3, 770-773.
- T. Wilk, S. Webster, H. Specht, G. Rempe, A. Kuhn, Polarization-Controlled Single Photons. *Phys. Rev. Lett.* **2007**, 98, 063601-4.
- Y. Masumoto, T. Takagahara. Semiconductor quantum dots: physics, spectroscopy and applications, Springer-Verlag : Berlin Heidelberg, **2002**.
- M. Sugisaki, H-W. Ren, K. Nishi, S. Sugou, Y. Masumoto. Excitons at a single localized center induced by a natural composition modulation in bulk Ga<sub>0.5</sub>In<sub>0.5</sub>P. *Phys. Rev. B* **2000**, 61, 16040-4; M. Sugisaki, H-W. Ren, S.V. Nair, J-S. Lee, S. Sugou, T. Okuno, Y. Masumoto. Imaging and single dot spectroscopy of InP self-assembled quantum dots. *J. Lumin.* **2000**, 87, 40-45.
- R. Yan, D. Gargas, P. Yang. Nanowire photonics. *Nat. Photonics* **2009**, 3, 569-576.
- P. Kamyczek, E. Placzek-Popko Z. R. Zytewicz, Z. Gumieny, E. Zielony, M. Sobanska, K. Klocek, A. Reszka. Structural and optical characterization of GaN nanowires. *J. Appl. Phys.* **2013**, 113, 204303-5.
- B. Liu, F.Yuan, B. Dierre, T. Sekiguchi, S. Zhang, Y. Xu, X. Ziang. Origin of yellow-band emission in epitaxially grown GaN nanowire arrays. *ACS Appl. Mater. Inter.* **2014**, 6, 14159-14166.
- X. Zhou, M.-Y. Lu, Y.-J. Lu, S. Gwo, S. Gradecak. Correlation of doping structure and carrier dynamics in a single GaN nanorod. *Appl. Phys. Lett.* **2013**, 102, 253104-5.
- O. Brandt, C. Pfüller, C. Chèze, L. Geelhaar, H. Riechert. Sub-meV linewidth of excitonic luminescence in single GaN nanowires: Direct evidence for surface excitons. *Phys. Rev. B* **2010**, 81, 045302-7.
- J.-B. Schlager, N.-A. Sanford, K.-A. Bertness, J.-M. Barker, A. Roshko, P.-T. Blanchard, Polarization-resolved photoluminescence study of individual GaN nanowires grown by catalyst-free molecular beam epitaxy. *Appl. Phys. Lett.* **2006**, 88, 213106-3.
- Q. Li, G. T. Wang. Spatial distribution of defect luminescence in GaN nanowires. *Nano Lett.* **2010**, 10, 1554-1558.
- A. H. Chin, T. S. Ahn, H. Li, S. Vaddiraju, C. J. Bardeen, C.-Z. Ning, M. K. Sunkara. Photoluminescence of GaN nanowires of different crystallographic orientations. *Nano Lett.* **2007**, 7, 626-631.
- J. Bruckbauer, P.R. Edwards, J. Bai, T. Wang, R.W. Martin. Probing light emission from quantum wells within a single nanorod. *Nanotechnology* **2013**, 24, 365704-7.
- T. Kuykendall, P. Ulrich, S. Aloni, P. Yang. Complete composition tunability of InGaN nanowires using a combinatorial approach. *Nat. Mater.* **2007**, 6, 951-956.
- Z. Liliental-Weber, D. N. Zakharov, M. Y. Kin, J. W. Ager, W. Walukiewicz, E. E. Haller, H. Lu, W. J. Schaff. Compositional modulation in In<sub>x</sub>Ga<sub>1-x</sub>N: TEM and X-ray studies. *J. Electron Microsc.* **2005**, 54, 243-250.
- F. Qian, Y. Li, S. Gradecak, D. Wang, C. J. Barrelet, C. M. Lieber. Gallium nitride-based nanowire radial heterostructures for nanophotonics. *Nano Lett.* **2004**, 4, 1975-1979.
- F. Qian, S. Gradecak, Y. Li, C. Y. Wen, C. M. Lieber. Core/multishell nanowire heterostructures as multicolor, high-efficiency light-emitting diodes. *Nano Lett.* **2005**, 5, 2287-2291.
- A. Motayed, A.V. Davydov, M. He, S. N. Mohammad, J. Melngailis. 365 nm operation of *n*-nanowire/*p*-gallium nitride homojunction light emitting diodes. *Appl. Phys. Lett.* **2007**, 90, 183120-3.
- H.-W. Lin, Y.-J. Lu, H.-Y. Chen, H.-M. Lee, S. Gwo, InGaN/GaN nanorod array white light-emitting diode. *Appl. Phys. Lett.* **2010**, 97, 073101-3.
- Y.-J. Lu, H.-W. Lin, H.-Y. Chen, Y.-C. Yang, S. Gwo. Single InGaN nanodisk light emitting diodes as full-color subwavelength light sources. *Appl. Phys. Lett.* **2011**, 98, 233101-3.

22. J. C. Johnson, H. J. Choi, K. P. Knutsen, R. D. Schaller, P. Yang, R. J. Saykally. Single gallium nitride nanowire lasers. *Nat. Mater.* **2002**, 1, 106-110.
23. F. Qian, Y. Li, S. Gradecak, H.G. Park, Y. Dong, Y. Ding, Z. L. Wang, C. M. Lieber. Multi-quantum-well nanowire heterostructures for wavelength-controlled lasers. *Nat. Mater.* **2008**, 7, 701-706.
24. A. Patsha, S. Amirthapandian, R. Pandian, S. Dhara. Influence of oxygen in architecting large scale nonpolar GaN nanowires. *J. Mater. Chem. C* **2013**, 1, 8086-8093.
25. P. Waltereit, O. Brandt, A. Trampert, H. Grahn, J. Menniger, M. Ramsteiner, M. Reiche, K. H. Ploog. Nitride semiconductors free of electrostatic fields for efficient white light-emitting diodes. *Nature* **2000**, 406, 865-868.
26. A. Pollard, N. Kumar, A. Rae, S. Mignuzzi, W. Su, D. Roy. Nanoscale Optical Spectroscopy: An Emerging Tool for the Characterisation of 2 D Materials. *J. Mat. NanoSci.*, **2014**, 1(1), 39-49.
27. E. Poliani, MR. Wagner, J.S. Reparaz, M. Mandl, M. Strassburg, X. Kong, A. Trampert, C. M. Sotomayor Torres, A. Hoffmann, J. Maultzsch. Nanoscale imaging of InN segregation and polymorphism in single vertically aligned InGaN/GaN multi quantum well nanorods by tip-enhanced Raman scattering. *Nano Lett.* **2013**, 13, 3205-3212.
28. A. Patsha, S. Amirthapandian, R. Pandian, S. Bera, A. Bhattacharya, S. Dhara. Direct evidence of mg incorporation pathway in vapor-liquid-solid grown p-type nonpolar GaN nanowires. *J. Phys. Chem. C.* **2014**, 118, 24165-24168.
29. A. Patsha, S. Dhara, A. K. Tyagi. Localized tip enhanced Raman spectroscopic study of impurity incorporated single GaN nanowire in the sub-diffraction limit. *Appl. Phys. Lett.* **2015**, 107, 123108-4.
30. P. Sahoo, S. Dhara, S. Dash, A. K. Tyagi, One dimensional GaN nanostructures: growth kinetics and applications. *Nanosci. Nanotechnol.-Asia* **2011**, 1, 140-161.
31. C.-L. Hsiao, L.-W. Tu, T.-W. Chi, M. Chen, T.-F. Young, C.-T. Chia, Y. M. Chang. Micro-Raman spectroscopy of a single freestanding GaN nanorod grown by molecular beam epitaxy. *Appl. Phys. Lett.* **2007**, 90, 043102-3.
32. J. Wang, F. Demangeot, R. Péchou, A. Ponchet, A. Cros, B. Daudin. Anticrossing of axial and planar surface-related phonon modes in Raman spectra of self-assembled GaN nanowires. *Phys. Rev. B*, **2012**, 85, 155432-6.
33. J. H. Zhu, J. Q. Ning, C. C. Zheng, S. J. Xu, S. M. Zhang, H. Yang. Localized surface optical phonon mode in the InGaN/GaN multiple-quantum-wells nanopillars: Raman spectrum and imaging. *Appl. Phys. Lett.* **2011**, 99, 113115-3.
34. S.-E. Wu, S. Dhara, T.-H. Hsueh, Y.-F. Lai, C.-Y. Wang, C.-P. Liu. Surface optical phonon modes in ternary aligned crystalline InGaN/GaN multi-quantum-well nanopillar arrays. *J. Raman Spectrosc.* **2009**, 40, 2044-2049.
35. P. Sahoo, J. Basu, S. Dhara, H.-C. Fang, C.-P. Liu, T. R. Ravindran, S. Dash, A. K. Tyagi. Single-step growth dynamics of core-shell GaN on Ga<sub>2</sub>O<sub>3</sub> freestanding nanoprotuded microbelts. *J. Mater. Sci.* **2011**, 47, 3447-3453.
36. T. Livneh, J. Zhang, G. Cheng, M. Moskovits. Polarized Raman scattering from single GaN nanowires. *Phys. Rev. B* **2006**, 74, 35320-10.
37. P. J. Pauzauskie, D. Talaga, K. Seo, P. Yang, F. Lagugné-Labarthe. Polarized Raman confocal microscopy of single gallium nitride nanowires. *J. Am. Chem. Soc.* **2005**, 127, 17146-17147.
38. A. Patsha, P. Sahoo, S. Dhara, S. Amirthapandian, A. K. Tyagi. Probing crystallographic orientation of a single GaN nanotube using polarized Raman imaging. *J. Raman Spectrosc.* **2013**, 44, 651-654.
39. S. Dhara, C. Y. Lu, C. T. Wu, C. W. Hsu, W. S. Tu, K. H. Chen, Y. L. Wang, L. C. Chen. Focused ion beam induced nanojunction and defect doping as a building block for nanoscale electronics in GaN nanowires. *J. Phys. Chem. C.* **2010**, 114, 15260-15265.
40. R. Calarco, M. Marso, T. Richter, A. I. Aykanat, R. Meijers, A. v. d. Hart, T. Stoica, H. Luth. Size-dependent photoconductivity in MBE-grown GaN-nanowires. *Nano Lett.* **2005**, 5, 981-984.
41. H.-Y. Chen, R.-S. Chen, N. K. Rajan, F.-C. Chang, L.-C. Chen, K.-H. Chen, Y.-J. Yang, M. A. Reed. A size-dependent persistent photocurrent and surface band bending in m-axial GaN nanowires. *Phys. Rev. B* **2011**, 84, 205443-7.
42. L. Vj, J. Oh, A. P. Nayak, A. M. Katzenmeyer, K. H. Gilchrist, S. Grego, N. P. Kobayashi, S.-Y. Wang. A perspective on nanowire photodetectors: Current status, future challenges, and opportunities. *IEEE J. Sel. Top. Quant.* **2011**, 17, 1002-1032.
43. R. S. Chen, S. W. Wang, Z. H. Lan, J.T. H. Tsai, C. T. Wu, L. C. Chen, K. H. Chen, Y.-S. Huang, C. C. Chen. On-chip fabrication of well-aligned and contact-barrier-free GaN nanobridge devices with ultrahigh photocurrent responsivity. *Small* **2008**, 4, 925-929.
44. M. D. Hertog, R. Songmuang, F. Gonzalez-Posada, E. Monroy. Single GaN based nanowires for photodetection and sensing applications. *Jpn. J. Appl. Phys.* **2013**, 52, 11NG01-11NG06.
45. A. D. L. Bugallo, L. Rigutti, G. Jacopin, F. H. Julien, C. Durand, X. J. Chen, D. Salomon, J. Eymery, M. Tchernycheva. Single-wire photodetectors based on InGaN/GaN radial quantum wells in GaN wires grown by catalyst-free metal-organic vapor phase epitaxy. *Appl. Phys. Lett.* **2011**, 98, 233107-3.
46. T. Westover, R. Jones, J. Huang, G. Wang, E. Lai, A. A. Talin. Photoluminescence, thermal transport, and breakdown in Joule-heated GaN nanowires. *Nano Lett.* **2008**, 9, 257-263.
47. M. D. Brubaker, P. T. Blanchard, J. B. Schlager, A. W. Sanders, A. Roshko, S. M. Duff, J. M. Gray, V. M. Bright, N. A. Sanford, K. A. Bertness. On-chip optical interconnects made with gallium nitride nanowires. *Nano Lett.* **2013**, 13, 374-377.
48. M. Tchernycheva, A. Messanvi, A. de Luna Bugallo, G. Jacopin, P. Lavenus, L. Rigutti, H. Zhang, Y. Halioua, F. H. Julien, J. Eymery, C. Durand. Integrated photonic platform based on InGaN/GaN nanowire emitters and detectors. *Nano Lett.* **2014**, 14, 3515-3520.
49. Y. J. Hwang, C. H. Wu, C. Hahn, H. E. Jeong, P. Yang. Si/InGaN core/shell hierarchical nanowire arrays and their photoelectrochemical properties. *Nano Lett.* **2012**, 12, 1678-1682.
50. B. AlOtaibi, M. Harati, S. Fan, S. Zhao, H. P. Nguyen, M. G. Kibria, Z. Mi. High efficiency photoelectrochemical water splitting and hydrogen generation using GaN nanowire photoelectrode. *Nanotechnology* **2013**, 24, 175401-5.
51. B. AlOtaibi, H.P. Nguyen, S. Zhao, M.G. Kibria, S. Fan, Z. Mi. Highly stable photoelectrochemical water splitting and hydrogen generation using a double-band InGaN/GaN core/shell nanowire photoanode. *Nano Lett.* **2013**, 13, 4356-4361.
52. K. Maeda, K. Teramura, D. Lu, T. Takata, N. Saito, Y. Inoue, K. Domen. Photocatalytic releasing hydrogen from water. *Nature* **2006**, 440, 295.
53. D.-H. Tu, H.-C. Wang, P.-S. Wang, W.-C. Cheng, K.-H. Chen, C.-I. Wu, S. Chattopadhyay, L. C. Chen. Improved corrosion resistance of GaN electrodes in NaCl electrolyte for photoelectrochemical hydrogen generation. *Int. J. Hydrogen Energy* **2013**, 38, 14433-14439.
54. P.-T. Chen, C.-L. Sun, M. Hayashi. First-principles calculations of hydrogen generation due to water splitting on polar GaN surfaces. *J. Phys. Chem. C.* **2010**, 114, 18228-18232.
55. X. Shen, Y. A. Small, J. Wang, P. B. Allen, M. V. Fernandez-Serra, M. S. Hybertsen, J. T. Kukerman. Photocatalytic water oxidation at the GaN (10-10) water interface. *J. Phys. Chem. C.* **2010**, 114, 13695-13704.
56. Y.-G. Lin, Y.-K. Hsu, A. M. Basilio, Y.-T. Chen, K.-H. Chen, L.-C. Chen. Photoelectrochemical activity on Ga-polar and N-polar GaN surfaces for energy conversion. *Opt. Express* **2014**, 22, A21-A27.
57. M. G. Kibria, S. Zhao, F. A. Chowdhury, Q. Wang, H. P. Nguyen, M. L. Trudeau, H. Guo, Z. Mi. Tuning the surface Fermi level on p-type gallium nitride nanowires for efficient overall water splitting. *Nat. Commun.* **2014**, 5, 3825-3826.
58. E. Trybus, G. Namkoong, W. Henderson, S. Burnham, W. A. Doolittle, M. Cheung, A. Cartwright. InN: A material with photovoltaic promise and challenges. *J. Cryst. Growth.* **2006**, 288, 218-224.
59. J. Wu, W. Walukiewicz, K. M. Yu, W. Shan, J. W. Ager II, E. E. Haller, H. Lu, W. J. Schaff, W. K. Metzger, S. Kurtz. Superior radiation

- resistance of  $\text{In}_{1-x}\text{Ga}_x\text{N}$  alloys: Full-solar-spectrum photovoltaic material system. *J. Appl. Phys.* **2003**, 94, 6477-6482.
60. J. F. Muth, J. H. Lee, I. K. Shmagin, R. M. Kolbas, H. C. Casey Jr., B. P. Keller, U. K. Mishra, S. P. DenBarrs. Absorption coefficient, energy gap, exciton binding energy, and recombination lifetime of GaN obtained from transmission measurements. *Appl. Phys. Lett.* **1997**, 71, 2572-2574.
  61. Y.B. Tang, Z.H. Chen, H.S. Song, C.S. Lee, H.T. Cong, H.M. Cheng, W. J. Zhang, I. Bello, S. T. Lee. Vertically aligned *p*-type single-crystalline GaN nanorod arrays on *n*-type Si for heterojunction photovoltaic cells. *Nano Lett.* **2008**, 8, 4191-4195.
  62. Y. Dong, B. Tian, T. J. Kempa, C. M. Lieber. Coaxial group III-nitride nanowire photovoltaics. *Nano. Lett.* **2009**, 9, 2183-2187.
  63. J. J. Wierer Jr., Q. Li, D. D. Koleske, S. R. Lee, G. T. Wang. III-nitride core-shell nanowire arrayed solar cells. *Nanotechnology* **2012**, 23, 194007-6.
  64. J. Bai, C.C. Yang, M. Athanasiou, T. Wang. Efficiency enhancement of InGaN/GaN solar cells with nanostructures. *Appl. Phys. Lett.* **2014**, 104, 051129-4.
  65. H. W. Seo, S. Y. Bae, J. Park, H. Yang, K. S. Park, S. Kim. Strained gallium nitride nanowires. *J. Chem. Phys.* **2002**, 116, 9492-9.
  66. A. Sanders, P. Blanchard, K. Bertness, M. Brubaker, C. Dodson, T. Harvey, W. J. Zhang, I. Bello, S. T. Lee. Homoepitaxial *n*-core: *p*-shell gallium nitride nanowires: HVPE overgrowth on MBE nanowires. *Nanotechnology* **2011**, 22, 465703-7.
  67. S. Gradecak, F. Qian, Y. Li, H.-G. Park, C. M. Lieber, GaN nanowire lasers with low lasing thresholds. *Appl. Phys. Lett.* **2005**, 87, 173111-3.
  68. H.-J. Choi, J. C. Johnson, R. He, S.-K. Lee, F. Kim, P. Pauzauskis, J. Golberger, R. J. Saykally, P. Yang. Self-organized GaN quantum wire UV lasers. *J. Phys. Chem. B.* **2003**, 107, 8721-8725.
  69. C.-Y. Wu, C.-T. Kuo, C.-Y. Wang, C.-L. He, M.-H. Lin, H. Ahn, S. Gwo. Plasmonic green nanolaser based on a metal-oxide-semiconductor structure. *Nano Lett.* **2011**, 11, 4256-4260.
  70. Y.-J. Lu, J. Kim, H.-Y. Chen, C. Wu, N. Dabidian, C. E. Sanders, C.-Y. Wang, M.-Y. Lu, B.-H. Li, X. Qiu, W.-H. Chang, L.-J. Chen, G. Shvets, C.-K. Shih, S. Gwo. Plasmonic nanolaser using epitaxially grown silver film. *Science* **2012**, 337, 450-453.
  71. Y.-J. Lu, C.-Y. Wang, J. Kim, H.-Y. Chen, M.-Y. Lu, Y.-C. Chen, W.-H. Chang, L.-J. Chen, M. I. Stockman, C.-K. Shih, S. Gwo. All-color plasmonic nanolasers with ultralow thresholds: Autotuning mechanism for single-mode lasing. *Nano Lett.* **2014**, 14, 4381-4388.
  72. P. Sahoo, S. Dhara, S. Amirthapandian, M. Kamruddin, S. Dash, B.K. Panigrahi, A. K. Tyagi. Role of surface polarity in self-catalyzed nucleation and evolution of GaN nanostructures. *Cryst. Growth Des.* **2012**, 12, 2375-2381.
  73. C. Y. Nam, D. Tham, J. E. Fischer. Effect of the polar surface on GaN nanostructure morphology and growth orientation. *Appl. Phys. Lett.* **2004**, 85, 5676-5678.
  74. R. Mata, A. Cros, K. Hestroffer, B. Daudin. Surface optical phonon modes in GaN nanowire arrays: Dependence on nanowire density and diameter. *Phys. Rev. B.* **2012**, 85, 035322-5.
  75. S. Sahoo, M.S. Hu, C. W. Hsu, C. T. Wu, K. H. Chen, L. C. Chen, A. K. Arora, S. Dhara. Surface optical Raman modes in InN nanostructures. *Appl. Phys. Lett.* **2008**, 93, 233116-3.
  76. K. K. Madapu, N. R. Ku, S. Dhara, C. P. Liu, A. K. Tyagi. Morphology of InN nanorods using spectroscopic Raman imaging. *J. Raman Spectrosc.* **2013**, 44, 791-794.
  77. P. Sahoo, S. Dhara, S. Dash, A.K. Tyagi, B. Raj, C.R. Das, P. Chandramohan, M.P. Srinivasan. Surface optical modes in GaN nanowires. *Int. J. Nanotechnol.* **2010**, 7, 823-832.
  78. S. Bhattacharya, A. Datta, S. Dhara, D. Chakravorty. Surface optical Raman modes in GaN nanoribbons. *J. Raman Spectrosc.* **2011**, 42, 429-433.
  79. S. Sahoo, S. Dhara, A.K. Arora, R. Krishnan, P. Chandramohan, M. P. Srinivasan. Raman scattering from surface optical phonon in diameter modulated AlN nanotips. *Appl. Phys. Lett.* **2010**, 96, 103113-3.
  80. S. Dhara, P. Sahoo, A. Tyagi, B. Raj. Surface Optical Mode in Semiconductor Nanowires. in *Nanowires-Implementation and Applications*. Ed. A. Hashim, Intech Open Access: Croatia, **2011**.
  81. H.-C. Hsu, G.-H. Hsu, Y.-S. Lai, Z.-C. Feng, S.-Y. Tseng, A. Lundskog, U. Forsberg, E. Janzén, K. H. Chen, L. C. Chen. Polarized and diameter-dependent Raman scattering from individual aluminum nitride nanowires: The antenna and cavity effects. *Appl. Phys. Lett.* **2012**, 101, 121902-5.
  82. A. Sivadasan, A. Patsha, S. Polaki, S. Amirthapandian, S. Dhara, A. Bhattacharya, B. K. Panigrahi, A. K. Tyagi. Optical properties of monodispersed AlGaIn nanowires in the single-prong growth mechanism. *Cryst. Growth Des.* **2015**, 15, 1311-1318.
  83. A. K. Sivadasan, A. Patsha, S. Dhara. Optically confined polarized resonance Raman studies in identifying crystalline orientation of sub-diffraction limited AlGaIn nanostructure. *Appl. Phys. Lett.* **2015**, 106, 173107-4.
  84. S. Lazić, E. Gallardo, J. Calleja, F. Agulló-Rueda, J. Grandal, M. Sánchez-García, E. Calleja, E. Luna, A. Trampert. Phonon-plasmon coupling in electron surface accumulation layers in InN nanocolumns. *Phys. Rev. B* **2007**, 76, 205319-6.
  85. A. Cros, Vibrational properties of semiconductor nanowires and nanowire heterostructures: ensembles and single nanowires. *phys. status. solidi. R* **2013**, 7, 727-738.
  86. R.-S. Chen, H.-Y. Chen, C.-Y. Lu, K.-H. Chen, C.-P. Chen, L.-C. Chen, Y.-J. Yang. Ultrahigh photocurrent gain in m-axial GaN nanowires. *Appl. Phys. Lett.* **2007**, 91, 223106-3.
  87. F. Gonzalez-Posada, R. Songmuang, M. Den Hertog, E. Monroy. Room-temperature photodetection dynamics of single GaN nanowires. *Nano Lett.* **2012**, 12, 172-176.
  88. R.-S. Chen, A. Ganguly, L.-C. Chen, K.-H. Chen. Recent advances in GaN nanowires: surface-controlled conduction and sensing applications. Ed. S. Pearton. *GaN and ZnO-based materials and devices*, Springer Science & Business Media, **2012**.
  89. R. Chen, H. Tsai, C. Chan, Y. Huang, Y. Chen, K. H. Chen, L. C. Chen. Comparison of CVD-and MBE-grown GaN nanowires: Crystallinity, photoluminescence, and photoconductivity. *J. Electron. Mater.* **2015**, 44, 177-187.
  90. H.-Y. Chen, R.-S. Chen, F.-C. Chang, L.-C. Chen, K.-H. Chen, Y.-J. Yang. *Appl. Phys. Lett.* **2009**, 95, 143123-3.
  91. A. Patsha, P. Sahoo, S. Amirthapandian, A. K. Prasad, A. Das, A. K. Tyagi, M. Cotta, S. Dhara. Localized charge transfer process and surface band bending in methane sensing by GaN nanowires. *J. Phys. Chem. C.* **2015**, 119, 21251-21260.
  92. R. S. Chen, H. Y. Tsai, Y. S. Huang, Y. T. Chen, L. C. Chen, K. H. Chen, Photoconduction efficiencies and dynamics in GaN nanowires grown by chemical vapor deposition and molecular beam epitaxy: A comparison study. *Appl. Phys. Lett.* **2012**, 101, 113109.
  93. N. A. Sanford, L. H. Robins, P.T. Blanchard, K. Soria, B. Klein, B. S. Eller, K. A. Bertness, J. B. Schlager, A. W. Sanders. Studies of photoconductivity and field effect transistor behavior in examining drift mobility, surface depletion, and transient effects in Si-doped GaN nanowires in vacuum and air. *J. Appl. Phys.* **2013**, 113, 174306-16.
  94. D. Feezell, Y. Sharma, S. Krishna. Optical properties of nonpolar III-nitrides for intersubband photodetectors. *J. Appl. Phys.* **2013**, 113, 133103-7.
  95. V.M. Ayres, B.W. Jacobs, Q. Chen, L. Udpa, Y. Fan, N. Tram, A. Baczewski, S. Kumar, M. Crimp, J. Halpern, M. He, M. A. Tupta, R. Stallcup, A. Hartman. Electronic transport characteristics of gallium nitride nanowire-based nanocircuits. *Nanotechnology* **2006**, *IEEE-NANO 2006*, **2006**, p. 496-499.
  96. D. Wang, A. Pierre, M. G. Kibria, K. Cui, X. Han, K. H. Bevan, H. Guo, S. Paradis, A. R. Hakima, Z. Mi. Wafer-level photocatalytic water splitting on GaN nanowire arrays grown by molecular beam epitaxy. *Nano Lett.* **2011**, 11, 2353-2357.
  97. K. Maeda, K. Teramura, N. Saito, Y. Inoue, K. Domen, Photocatalytic overall water splitting on Gallium nitride powder. *Bull. Chem. Soc. Jpn.* **2007**, 80, 1004-1410.

98. M. G. Kibria, H. P. Nguyen, K. Cui, S. Zhao, D. Liu, H. Guo, M. L. Trudeau, S. Paradis, A.-R. Hakima, Z. Mi. One-step overall water splitting under visible light using multiband InGaN/GaN nanowire heterostructures. *ACS Nano* **2013**, 7, 7886-7888.
99. L. Caccamo, J. Hartmann, C. Fabrega et al.. Band engineered epitaxial 3D GaN-InGaN core-shell rod arrays as an advanced photoanode for visible-light-driven water splitting. *ACS Appl. Mater. Interfaces* **2014**, 6, 2235-2240.
100. J. S. Hwang, T. Y. Liu, S. Chattopadhyay et al.. Growth of beta-Ga<sub>2</sub>O<sub>3</sub> and GaN nanowires on GaN for photoelectrochemical hydrogen generation. *Nanotechnology* **2013**, 24, 055401-10.
101. S. Fan, B. AlOtaibi, S.Y. Woo, Y. Wang, G.A. Botton, Z. Mi. High efficiency solar-to-hydrogen conversion on a monolithically integrated InGaN/GaN/Si adaptive tunnel junction photocathode. *Nano Lett.* **2015**, 15, 2721-2726.
102. J. Wallys, S. Hoffmann, F. Furtmayr, J. Teubert, M. Eickhoff. Electrochemical properties of GaN nanowire electrodes-influence of doping and control by external bias. *Nanotechn.* **2012**, 23, 165701-7.
103. Y.-F. Huang, S. Chattopadhyay, Y.-J. Jen et. al.. Improved broadband and quasi-omnidirectional anti-reflection properties with biomimetic silicon nanostructures. *Nat. Nanotechnol.* **2007**, 2, 770-774.
104. S. Funk, B. Hokkanen, U. Burghaus, A. Ghicov, P. Schmuki, Unexpected adsorption of oxygen on TiO<sub>2</sub> nanotube arrays: Influence of crystal structure. *Nano Lett.* **2007**, 7, 1091-1094.
105. M. Law, L. E. Greene, J. C. Johnson, R. Saykally, P. Yang. Nanowire dye-sensitized solar cells. *Nat. Mater.* **2005**, 4, 455-459.
106. B. Tian, X. Zheng, T. J. Kempa, Y. Fang, N. Yu, G. Yu, J. Huang, C. M. Lieber. Coaxial silicon nanowires as solar cells and nanoelectronic power sources. *Nature* **2007**, 449, 885-889.
107. A. Patsha, R. Pandian, S. Dhara, A. K. Tyagi. Nonpolar p-GaN/n-Si heterojunction diode characteristics: A comparison between ensemble and single nanowire devices. *J. Phys. D: Appl. Phys.* **2015**, 48, 395102-395107.

## AUTHORS BIOGRAPHY



**Avinash Patsha** studied M.Sc., Physics at Banaras Hindu University, Varanasi and received his Ph.D. (Physics) degree from Homi Bhabha National Institute, Kalpakkam, India. He performed his doctoral research on the effect of impurities on physical and chemical properties of GaN nanowires synthesized by atmospheric pressure chemical vapor deposition technique. His research interests are mainly in the plasmonic and semiconductor nanostructures for electronic and optoelectronic applications. Currently, he is a postdoctoral research fellow under Pikovsky Valazzi matching scholarship at Tel-Aviv University, Israel.



**Prof. Sandip Dhara** is a Fellow of Royal Society of Chemistry, FRSC and recipient of Department of Atomic Energy-Scientific Research Council (DAE-SRC) Outstanding Researcher Award in the year 2012. He studied M.Sc. Physics at Indian Institute of Technology, Kharagpur, India (1988) and received his Ph.D. (Physics) degree from Birla Institute of Technology and Science, Pilani, India in 1994. His research interests are mainly in the field of growth and defect study in single 1-D nanostructure and Light-Matter Interaction at Nanoscale using near field scanning optical microscopy (NSOM), and utilizing tip enhanced Raman spectroscopy (TERS) in the sub-diffraction limit. He has published 6 books chapters/review articles and over 200 papers, with an H-index of 25. He is currently the Head of Surface and Nanoscience Division, Materials Science Group, IGCAR, Kalpakkam. He is also affiliated to Homi Bhabha National Institute, Deemed University, India.



**Prof. Surojit Chattopadhyay** is a Ph.D. in Physics, from University of Calcutta, India, and is currently working in National Yang Ming University. Previously, he has worked in the thin film coatings industry. He had received the Chevening Scholarship from the Govt. of UK. His current research interests include novel, and functional nanomaterials for applications in optoelectronics, such as photodetectors, and biomedical field including drug delivery, phototherapy, bioimaging, among others. He has published over 75 papers in international peer reviewed journals.



**Prof. Kuei-Hsein Chen** received B.S. in Physics from National Taiwan University (1981), and Ph.D. in Applied Physics from Harvard University (1989). He was Scientific Researcher, in General Electric R&D, Schenectady, New York (1990 - 1992). His group is specialized in nanomaterials and their applications for catalysis and energy conversion. He has published over 400 papers, with an H-index of 60. He has received a number of awards, such as Outstanding Research Award, National Science Council, Taiwan (2005), Outstanding Scholar Award, Foundation for the Advancement of Outstanding Scholarship (2008), and Material Science Award under Jin-Duei Ho Fundation Award (2013). He is currently the Director of Institute of Atomic and Molecular Sciences, Academia Sinica, Taiwan. He is also Adjunct Research Fellow, Center for Condensed Matter Sciences, National Taiwan University, Taipei, Taiwan (since 2002).



**Prof. Li-Chyong Chen** received B.S. in Physics from National Taiwan University (1981), and Ph.D. in Applied Physics from Harvard University (1989). Her group is specialized in low-dimensional nanomaterials and their applications for energy, optoelectronics, and sensing. Till date she has 15 patents, 15 book chapters/review articles and over 390 papers, with an H-index of 62. Dr. Chen is a Fellow of both the Physical Society of Taiwan and the Materials Research Society (MRS) in USA. She has received a number of domestic and international awards, such as twice the Ministry of Science and Technology Outstanding Research Award, Ho Chin-Tui Foundation Outstanding Scholar Award, Laureate of the 22<sup>nd</sup> Khwarizmi International Award (Iran), Acharya Vinova International Award in Materials Science and Technology, Academician of Asia Pacific Academy of Materials, and the Taiwan Outstanding Women in Science. Most recently, she is elected as a Board of Director for the MRS for 3 yrs (2017-20).